

Efficient bayesian multi-view deconvolution

Stephan Preibisch^{1,2,3}, Fernando Amat², Evangelia Stamatakis¹, Mihail Sarov¹, Eugene Myers^{1,2} and Pavel Tomancak¹

¹Max Planck Institute of Molecular Cell Biology and Genetics, 01307 Dresden, Germany

²Janelia Farm Research Campus, Howard Hughes Medical Institute, Ashburn, VA 20147, USA

³Department of Anatomy and Structural Biology, Gruss Lipper Biophotonics Center, Albert Einstein College of Medicine, Bronx, NY 10461, USA

Correspondence should be addressed to: preibischs@janelia.hhmi.org and tomancak@mpi-cbg.de

Abstract

Light sheet fluorescence microscopy is able to image large specimen with high resolution by imaging the samples from multiple angles. Multi-view deconvolution can significantly improve the resolution and contrast of the images, but its application has been limited due to the large size of the datasets. Here we present a derivation of multi-view Bayesian deconvolution that drastically improves the convergence time and provide a GPU implementation that optimizes runtime performance.

Modern light sheet microscopes^{1,2,3} are able to acquire large, developing specimens with high temporal and spatial resolution typically by imaging them from multiple directions. The low photodamage offered by a light sheet microscope's design allows the recording of massive, time-lapse datasets that have the potential to enable the reconstruction of entire lineage trees of the developing specimen. However, accurate segmentation and tracking of nuclei and cells in these datasets remain a challenge because image quality is limited by the optical properties of the imaging system and the compromises between acquisition speed and resolution. Deconvolution utilizes knowledge about the optical system to substantially increase spatial resolution and contrast after acquisition. An advantage unique to light sheet microscopy and in particular to Selective Plane Illumination Microscopy (SPIM), is the ability to observe the same location in the specimen from multiple angles which renders the ill-posed problem of deconvolution more tractable⁴⁻¹¹.

Richardson-Lucy deconvolution^{12,13} (**Suppl. Note Chapter 1 and 2**) is a Bayesian expectation-maximization algorithm¹⁴ that is often chosen for its simplicity and performance. It has previously been extended to multi-view geometry (**Fig. 1a,b** and **Suppl. Note Chapter 3**)^{9,11}, however the convergence time of the algorithm remains orders of magnitude longer than the time required to record the data. We address this problem by deriving an optimized formulation of Bayesian deconvolution for multiple view geometry that explicitly incorporates conditional probabilities between the views (**Fig. 1c**) and an optimized iteration scheme achieving significantly faster convergence (**Fig. 1d,e**).

Bayesian deconvolution models images and point spread functions (PSFs) as probability distributions. The goal is to estimate the most probable underlying distribution (deconvolved image) that explains best all observed distributions (views) given their conditional probabilities (PSFs). Following the notation of Lucy¹³ **Suppl. Note Chapter 2** re-derives the original Richardson-Lucy deconvolution algorithm that is subsequently extended to multiple-view geometry. **Suppl. Note Chapter 3** provides the first complete derivation of Richardson-Lucy multi-view deconvolution based on probability theory and Bayes' theorem

$$\psi^{r+1}(\xi) = \psi^r(\xi) \prod_{v \in V} \int_{x_v} \frac{\phi_v(x_v)}{\int_{\xi} \psi^r(\xi) P(x_v|\xi) d\xi} P(x_v|\xi) dx_v \quad (1)$$

Previous extensions to multiple views^{9,11} were based on the assumption that the individual views are independent observations. Assuming independence between two views implies that by observing one view, nothing can be learned about the other view. In **Suppl. Note Chapter 4** we show that this independence assumption is not required, and thereby prove that the above equation for 'classical' Bayesian multi-view deconvolution is correct and not an approximation as previously assumed.

As we do not need to consider views to be independent, we are asking if the conditional probabilities describing the relationship between two views can be modeled and used in order to improve convergence behavior (**Suppl. Note Chapter 5**). We argue that it is possible to estimate from one view the upper boundary for another view in case the PSF's of both views are known. If we consider a single photon observed in the first view, the first PSF and Bayes' theorem can be used to assign a probability to every location of the underlying distribution having emitted this photon (**Supplementary Fig. 1b**). Based on this probability distribution, the second PSF directly yields the probability distribution describing where to expect a corresponding observation for the same

fluorophore in the second view. Therefore, our estimation of a second view is practically a twice blurred version of the first view (**Supplementary Fig. 2**).

We use these ‘virtual’ views to perform intermediate update steps at no additional computational cost (**Suppl. Note Chapter 5, Supplementary Fig. 3**) decreasing the computational effort approximately 2-fold (**Fig. 1b-d**). We show that by additionally replacing the combined multiplicative update scheme used in conventional multi-view deconvolution (**Fig. 1b**) with sequential updates (**Fig. 1c** and **Suppl. Note Chapter 7**) the convergence time decreases 13-fold and this gain increases with the number of views (**Fig. 1d** and **Suppl. Note Chapter 8**). The new algorithm performs well in the presence of noise (**Suppl. Note Chapter 9, Supplementary Fig. 6, 7**) and imperfect point spread functions (**Suppl. Note Chapter 10, Supplementary Fig. 8, 9**). To further reduce convergence time we introduce ad-hoc simplifications (optimization I & II) for the estimation of conditional probabilities (**Suppl. Note Chapter 6**), which, in the absence of noise, achieve up to 40-fold improvement compared to deconvolution methods that assume view independence (**Fig. 1d, Supplementary Fig. 4**). As a compromise between quality and speed we use, if not stated otherwise, the intermediate optimization I (**Fig. 1d,e** and **Suppl. Note Chapter 6.1**) for all deconvolution experiments on real datasets.

Prerequisite for multi-view deconvolution of light sheet microscopy data are precisely aligned multi-view datasets and estimates of point spread functions for all views. We exploit the fact that for the purposes of registration we include sub-resolution fluorescent beads into the rigid agarose medium in which the specimen is embedded. The beads are initially used for multi-view registration of the SPIM data¹⁵ and subsequently to extract the PSF for each view for the purposes of multi-view deconvolution. We average the intensity of PSFs for each view for all the beads that were identified as corresponding during registration yielding a precise measure of the PSF for each view under the specific experimental condition. This synergy of registration and deconvolution ensures realistic representation of PSFs under any imaging condition. Alternatively, simulated PSFs or PSFs measured by other means can be provided as inputs to the deconvolution algorithm.

We applied the multi-view deconvolution to multi-view SPIM acquisitions of *Drosophila* and *C. elegans* embryos (**Fig. 2a-e**). We achieve a significant increase in contrast as well as resolution with respect to the content-based fusion¹⁵ (**Fig. 2b**) while only a few iterations are required and computation times are typically in the range of a few minutes per multi-view acquisition (**Supplementary Table 1**). A remaining challenge for creating a complete computational model of *C. elegans* larvae in L1 stage is to be able to identify all nuclei in the nervous system¹⁶. We applied the deconvolution to a 4-view acquisition of a fixed specimen expressing GFP tagged lamin (LMN-1::GFP) labeling the nuclear lamina and stained for DNA with Hoechst (**Fig. 2f,g**). Running the multi-view deconvolution for 100 iterations using optimization II, we achieve a significantly improved contrast and resolution compared the input data acquired with the Zeiss Lightsheet Z.1 microscope (**Supplementary Video 5-7**). Only the deconvolved dataset allows the manual segmentation of all 558 nuclei with uncertainty of about 5 nuclei among annotation trials (**Supplementary Video 8**).

The increased contrast and resolution are especially visible on samples acquired with thicker light sheets such as in the case of OpenSPIM¹⁷ (**Supplementary Fig. 10**). Out-of-focus light is significantly reduced and individual nuclei become separable even in orientations perpendicular to the rotation axis that have not been imaged by the microscope directly. Also very large datasets, such as the acquisition of *Drosophila* ovaries, with input data of over 5 billion voxels become computable in reasonable time (**Supplementary Fig. 11** and **Supplementary Table 1**). To further substantiate the utility of the algorithm we deconvolved an entire time-course of *Drosophila* embryonic development consisting of 236 time-points (**Supplementary Video 2-4**). The computation time was 24 hours using two Nvidia Quadro 4000 graphics cards, highlighting the performance and applicability of the method to very large datasets.

A major obstacle for widespread application of deconvolution approaches to multi-view light sheet microscopy data is lack of usable and scalable multi-view deconvolution software. We integrated our fast converging algorithm into Fiji's¹⁸ multi-view processing pipeline as open-source plugin where it complements existing approaches to multi-view data registration (http://fiji.sc/Multi-View_Deconvolution). We provide an efficient implementation for GPU and CPU taking advantage of ImgLib¹⁹. It offers processing times of a few minutes (**Fig. 1e** and **Supplementary Table 1**), comparable to the acquisition rates of common light sheet microscopes such as OpenSPIM or Lightsheet Z.1 (Carl Zeiss Microimaging). The long-term time-lapse acquisitions derived from Lightsheet Z.1 are truly massive (2.16 TB for 6 view 715 timepoint *Drosophila* embryogenesis recording) but our deconvolution plugin can process them in parallel on a computer cluster in real time (**Supplementary Video 9**). To account for potential noise in the input images we added an option for Tikhonov regularization²⁰ (**Supplementary Fig. 6,7**). The deconvolution can be processed on the entire image at once for optimal performance or in blocks to reduce the memory requirements. The only free parameter of the method that must be chosen by the user is the number of iterations for the deconvolution process (**Supplementary Fig. 4,5**). We facilitate this choice by providing a debug mode allowing the user to inspect all intermediate iterations and identify optimal tradeoff between quality and computation time. For a typical multi-view acquisition comprising 6–8 views we suggest between 10-15 iterations.

One of the challenges in image deconvolution is to arrive at the correct solution quickly without compromising quality. We have achieved significant improvement in convergence time over existing methods by exploiting conditional probabilities between views in a multi-view deconvolution scenario. We have further implemented the algorithm as an open source GPU accelerated software in Fiji where it synergizes with other related plugins into an integrated solution for the processing of multi-view light sheet microscopy data of arbitrary size.

Acknowledgements

We thank Tobias Pietzsch for very helpful discussions, proofreading and access to his unpublished software, Nathan Clack, Fernando Carrillo Oesterreich and Hugo Bowne-Anderson for discussions, Michael Weber for imaging the *Drosophila* time series, Steffen Jaensch for preparing the *C. elegans* embryo, Jun Kelly Liu for the LW698 strain, Stephan Saalfeld for help with 3D rendering and Carl Zeiss Microimaging for providing us with the SPIM prototype. S.P. was supported by MPI-CBG, HHMI and the Human Frontier Science Program (HFSP) Postdoctoral Fellowship. F.A. was supported by HHMI. G.M. was supported by HHMI and MPI-CBG. P.T. was supported by The European Research Council Community[2032?]'s Seventh Framework Program (FP7/2007-2013) grant agreement 260746.

Author contributions

S.P. and F.A. derived the equations for multi-view deconvolution. S.P. implemented the software and performed all analysis, F.A. implemented the GPU code. E.S. generated and imaged H2Av-mRFP Ruby fly line. M.S. prepared and M.S. and S.P. imaged the *C. elegans* L1 sample. S.P. & P.T. conceived the idea and wrote the manuscript. G.M. & P.T. supervised the project.

References

1. Huiskens, J. et al. Science 305(5686):1007-9 (2004)
2. Keller P.J. Science 322(5904):1065-9 (2008)
3. Truong et al. Nature Methods 8(9):757–760 (2011)
4. Swoger et al. Optics Express 15(13):8029-8042 (2007)
5. Harikumar et al. IEEE TIP 8(6):846-862 (1999)

6. Blume et al. MICAAI 10(1):743-750 (2007)
7. Rajagopalan et al. IEEE TIP 7(7):1075-1079 (1998)
8. Sroubek et al. IEEE TIP 12(9):1094-1106 (2003)
9. Krzic, Phd Thesis (2009)
10. de Vieilleville et al. IEMBS 4872-4875 (2011)
11. Temerinac-Ott et al. IEEE TIP 21(4):1863-1873 (2012)
12. Richardson et al. JOSA 62(1):55-59 (1972)
13. Lucy et al. Astronomical Journal 79(6):745-754 (1974)
14. Dempster et al. J. Roy. Statist. Soc. Ser. B 39(1):1-38 (1977)
15. Preibisch et al. Nature Methods 7(6):418-9 (2010)
16. Long et al. Nature Methods 6(9):667-672 (2009)
17. Pitrone et al. Nature Methods 10(7), 598–599 (2013)
18. Schindelin et al. Nature Methods 9(7):676-82 (2012)
19. Pietzsch et al. Bioinformatics 28(22):3009-3011 (2012)
20. Tikhonov et al. Washington: Winston & Sons (1977)

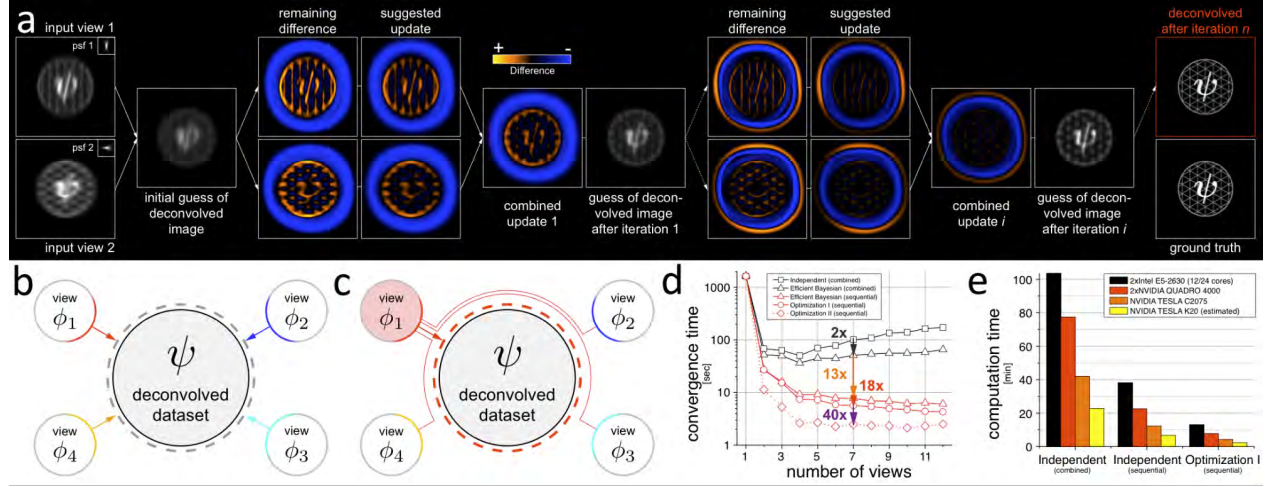


Figure 1: *Principles and performance* (a) Illustrates the basic workflow of the multi-view deconvolution on 2 views. First, each view computes the difference between the input and the current guess of the deconvolved image convolved with the PSF. Based on this it computes an update either taking into account conditional probabilities as pictured in (c) or assuming independence pictured in (b). The updates are then either combined and then applied or the individual update steps are applied directly (not shown). (b) Illustrates the ‘classical’ multi-view deconvolution^{9,11} where an update step is computed individually for each view and subsequently combined into one single update of the deconvolved image. (c) Illustrates our new derivation taking into account the conditional probabilities between the views. Each individual update step takes into account the other views using ‘virtual views’ and updates the deconvolved image individually, i.e. updates are performed sequentially and not combined. (d) Compares the convergence time of the different methods. We used a known ground truth image (**Supplementary Fig. 3**) and let all variations converge until they reach precisely the same quality. Note that the increase in computation time for an increasing number of views of the combined methods (black) is due to the fact that with an increasing number of views more computational effort is required to perform one update of the deconvolved image (**Supplementary Fig. 2**) (e) Computation times on CPU and different GPU hardware for the *Drosophila* dataset pictured in **Fig. 2c-e**. The input data are 7 views, each 720x380x350px.

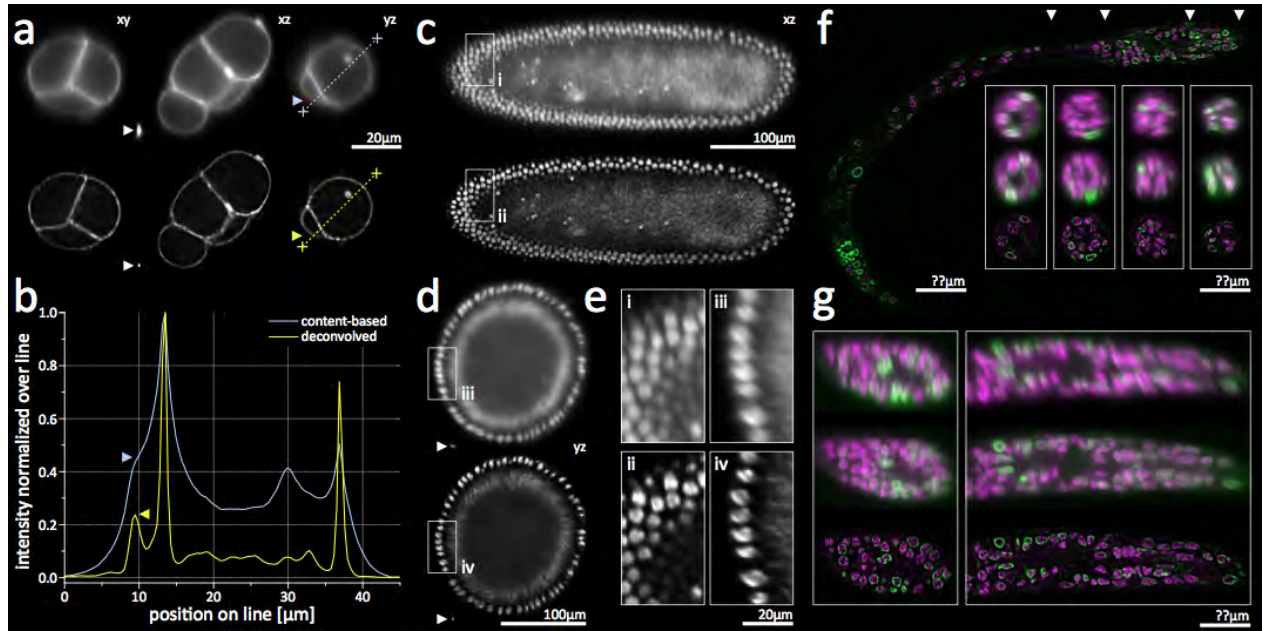


Figure 2: *Application to biological data* (a) Comparison of reconstruction results using content-based fusion (upper row) and multi-view deconvolution (lower row) on a 4-cell stage *C. elegans* embryo expressing PH-domain-GFP fusion marking the membranes. Dotted lines mark plots shown in (b), white arrows mark PSFs of a fluorescent bead before and after deconvolution. (b) Line plot through the volume along the rotation axis (yz), typically showing lowest resolution in light sheet acquisitions. Contrast along the line is locally normalized. Signal-to-noise is significantly enhanced, arrows mark points that illustrate increased resolution. (c,d) show cut planes through a blastoderm stage *Drosophila* embryo expressing His-YFP in all cells. White boxes mark areas magnified in (e). Detailed comparison of computation times for this dataset is shown in **Fig 1e**. (e) Magnified view on small parts of the *Drosophila* embryo. Left panel shows one of the directly acquired views, right panel shows a view along the rotation axis usually characterized by the lowest resolution. (f,g) Comparison of the deconvolved image data to the input data of a fixed *C. elegans* larvae in L1 stage expressing LMN-1-GFP (green) and stained with Hoechst (magenta). (f) Single slice through the deconvolved dataset, arrows mark 4 locations of transversal cuts shown below. The cuts compare two orthogonal input views (0, 90 degrees) with the deconvolved data. Note that no input view offers high resolution in this orientation approximately along the rotation axis. (g) The first row of the left box shows a random slice of a view in axial orientation marking the worst possible resolution of the microscope. The second row shows an input view in lateral orientation, i.e. the best possible resolution achieved by the microscope. The third row shows the corresponding deconvolved image. The box on the right shows a random slice through the nervous system. Note that the alignment of the *C. elegans* L1 dataset was refined using nuclear positions as described in **Supp. Note Chapter 12**.

Efficient Bayesian Multi-View Deconvolution

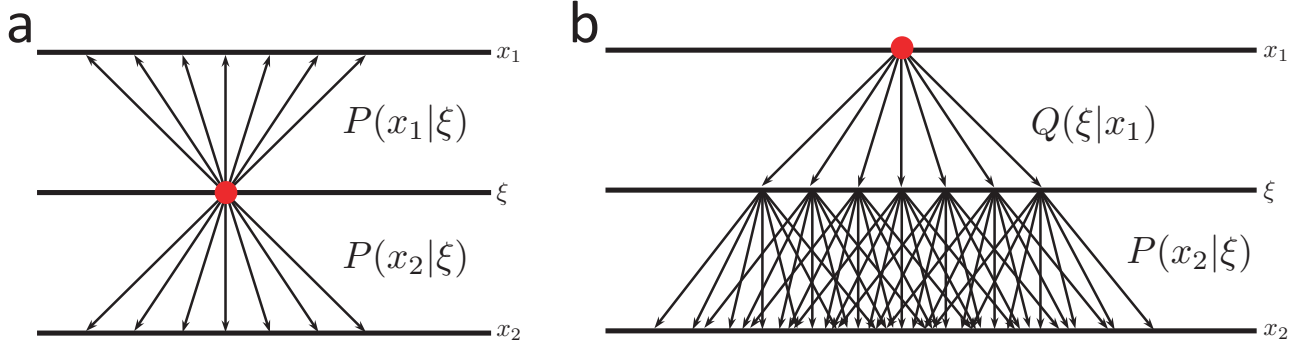
Stephan Preibisch*, Fernando Amat, Evangelia Stamatakis,
Mihail Sarov, Gene Myers and Pavel Tomancak*

Supplementary File	Title
Supplementary Figure 1	Illustration of conditional probabilities describing the dependencies of two views
Supplementary Figure 2	Illustration of 'virtual' views
Supplementary Figure 3	Illustration of assumption required for incorporating 'virtual' views without additional computational effort
Supplementary Figure 4	Performance comparison of the multi-view deconvolution methods and dependence on the PSF
Supplementary Figure 5	Images used for analysis and visual performance
Supplementary Figure 6	Effect of noise on the deconvolution results
Supplementary Figure 7	Intermediate stages of deconvolution results for varying SNR's and regularization
Supplementary Figure 8	Quality of deconvolution for imprecise estimation of the PSF
Supplementary Figure 9	Variation of the PSF across the light sheet in SPIM acquisitions
Supplementary Figure 10	Quality of reconstruction for an OpenSPIM acquisition of Drosophila embryo
Supplementary Figure 11	Quality of reconstruction of Drosophila ovaries
Supplementary Table 1	Summary of datasets used in this publication
Supplementary Note	Detailed derivations and discussion of the efficient Bayesian multi-view deconvolution

Note: Supplementary Video 1-9 are available for download on the Nature Methods homepage.

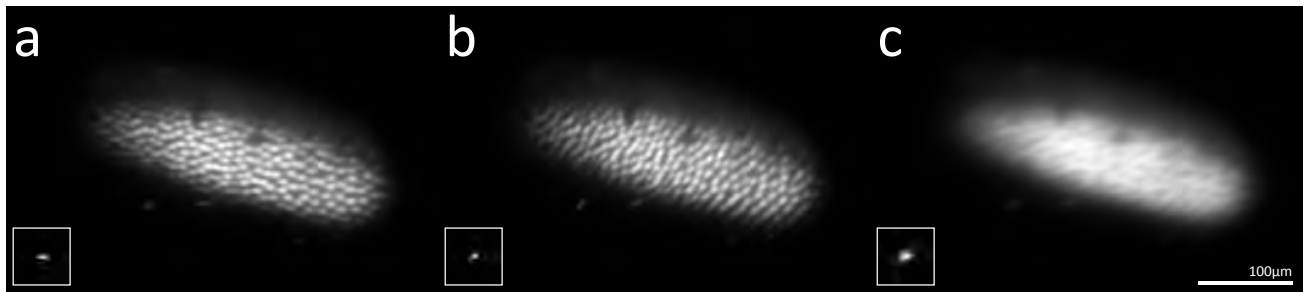
SUPPLEMENTARY FIGURES

SUPPLEMENTARY FIGURE 1 — Illustration of conditional probabilities describing the dependencies of two views



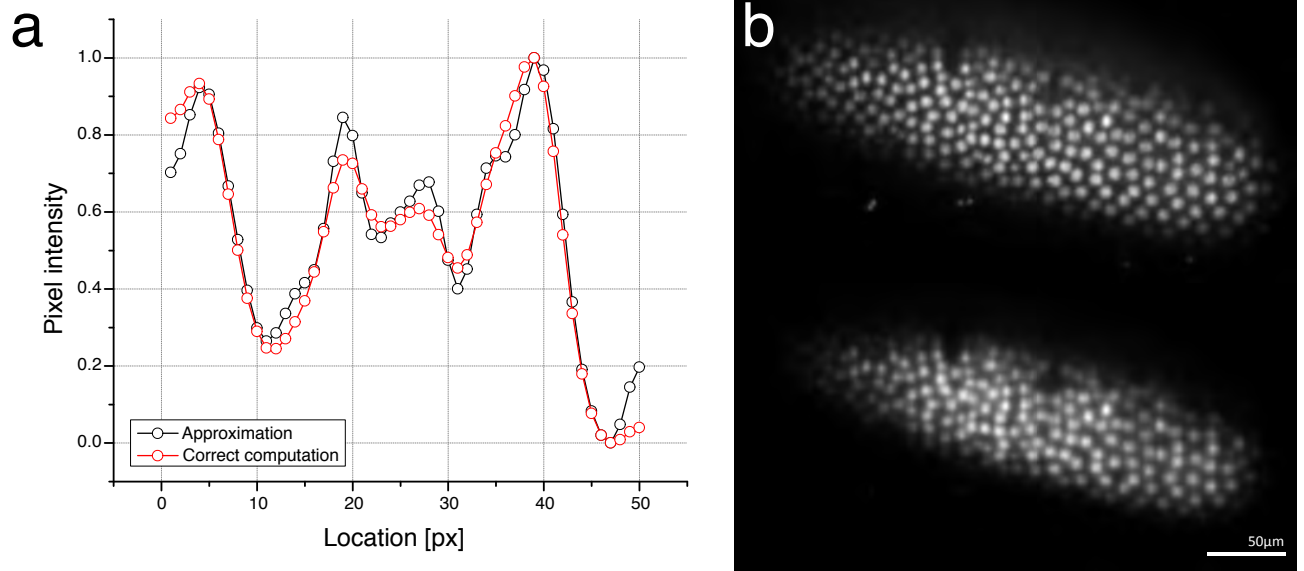
Supplementary Figure 1: *Illustration of conditional probabilities describing the dependencies of two views.* (a) illustrates the conditional independence of two observed distributions $\phi_1(x_1)$ and $\phi_2(x_2)$ if it is known that the event $\xi = \xi'$ on the underlying distribution $\psi(\xi)$ occurred. Given $\xi = \xi'$, both distributions are conditionally independent, the probability where to expect an observation only depends on $\xi = \xi'$ and the respective individual point spread function $P(x_1|\xi)$ and $P(x_2|\xi)$, i.e. $P(x_1|\xi, x_2) = P(x_1|\xi)$ and $P(x_2|\xi, x_1) = P(x_2|\xi)$. (b) illustrates the relationship between an observed distribution $\phi_2(x_2)$ and $\phi_1(x_1)$ if the event $x_1 = x'_1$ occurred. Solely the 'inverse' point spread function $Q(\xi|x_1)$ defines the probability for any event $\xi = \xi'$ to have caused the observation $x_1 = x'_1$. The point spread function $P(x_2|\xi)$ consecutively defines the probability where to expect a corresponding observation $x_2 = x'_2$ given the probability distribution $\psi(\xi)$.

SUPPLEMENTARY FIGURE 2 — Illustration of 'virtual' views



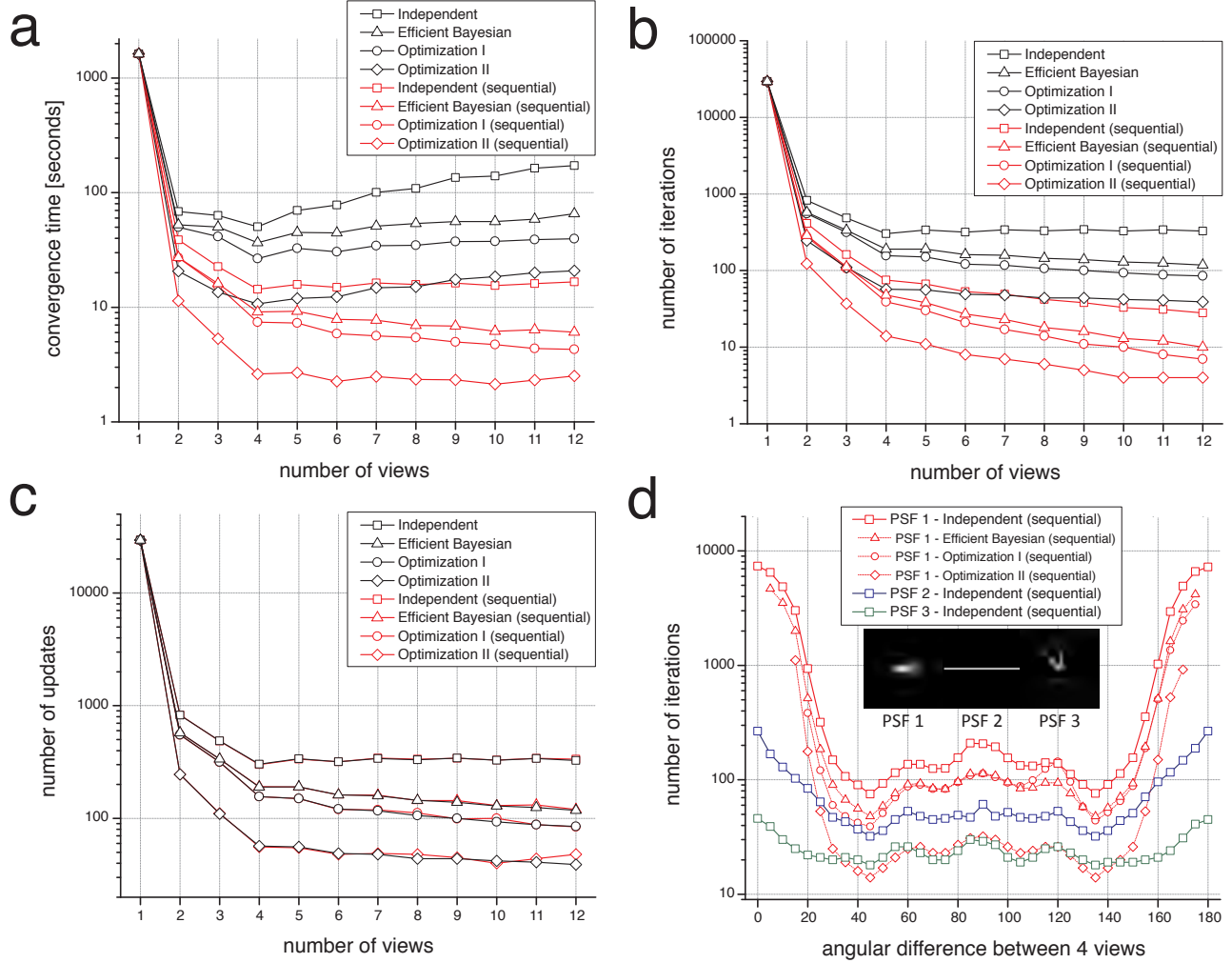
Supplementary Figure 2: *Illustration of virtual views.* (a,b) Two observed distributions (views) $\phi_1(x_1)$ and $\phi_2(x_2)$ as well as the corresponding PSF's $P(x_1|\xi)$ and $P(x_2|\xi)$. They show one slice of a *Drosophila* embryo expressing His-YFP in all cells, both views are based on the same ground truth picture used for simulations as shown in supplementary figure 5a. (c) The 'virtual' second distribution $\phi_2^V(x_1)$ simulates (b) using the image from (a) and both PSF's from (a) and (b). The effective PSF used for the simulation is shown in the bottom left. This observation $\phi_1^{V2}(x_2)$ can be seen as the upper boundary of $\phi_2(x_2)$ and summarizes our knowledge about view 2 by only observing view 1 and the knowledge of the PSF's.

SUPPLEMENTARY FIGURE 3 — Illustration of assumption required for incorporating 'virtual' views without additional computational effort



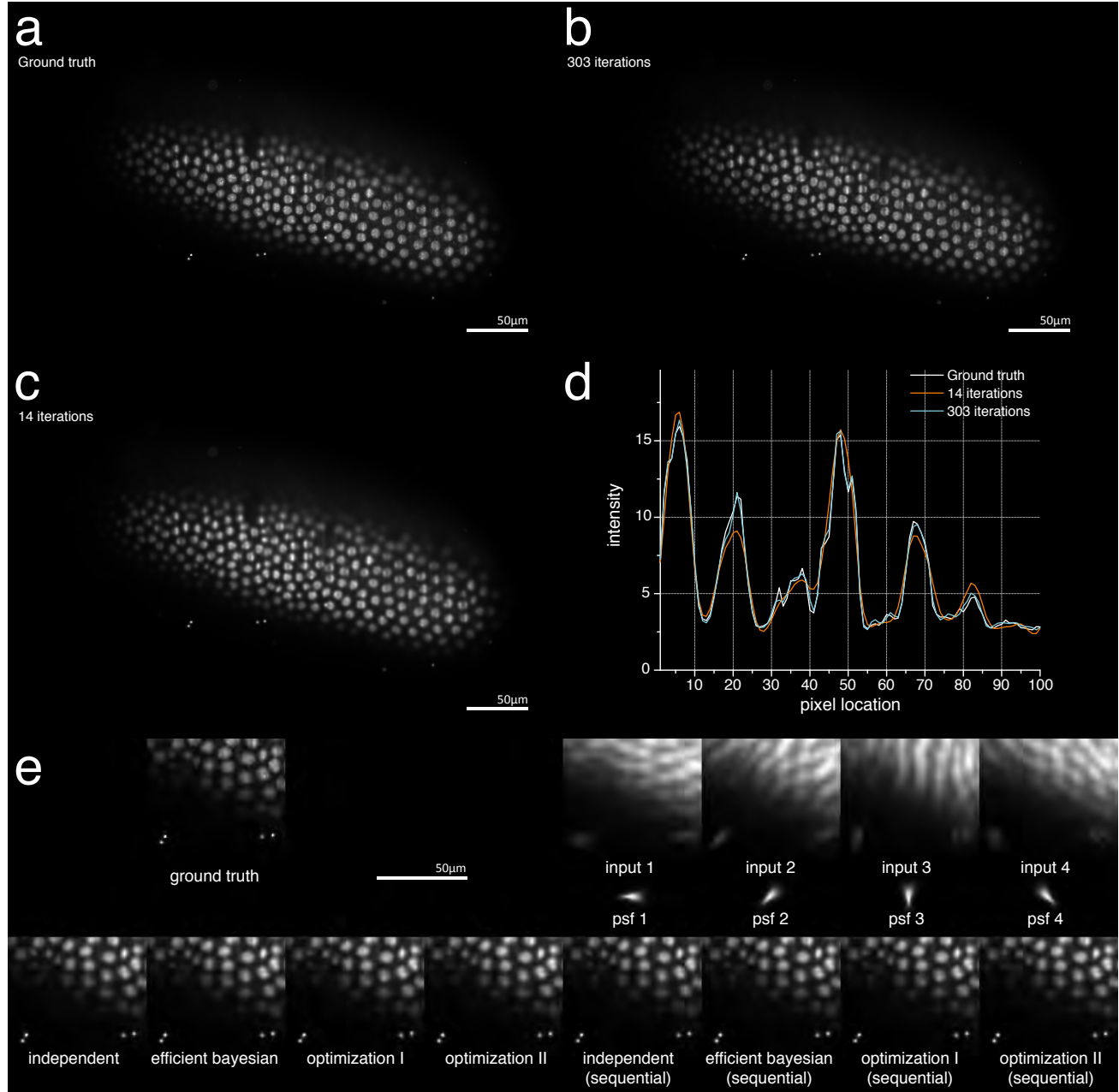
Supplementary Figure 3: *Illustration of assumption in equation 67.* (a) shows the difference in the result when computing $(f * g) \cdot (f * h)$ in red and the approximation $f * (g \cdot h)$ in black for a random one-dimensional input sequence (f) and two kernels with $\sigma=3$ (g) and $\sigma=2$ (h) after normalization. (b) shows the difference when using the two-dimensional image from supplementary figure 5a as input (f) and the first two point spread functions from supplementary figure 5e as kernels (g, h). The upper panel pictures the approximation, the lower panel the correct computation. Note that for (a,b) the approximation is slightly less blurred. Note that the beads are also visible in the lower panel when adjusting the brightness/contrast.

SUPPLEMENTARY FIGURE 4 — Performance comparison of the multi-view deconvolution methods and dependence on the PSF



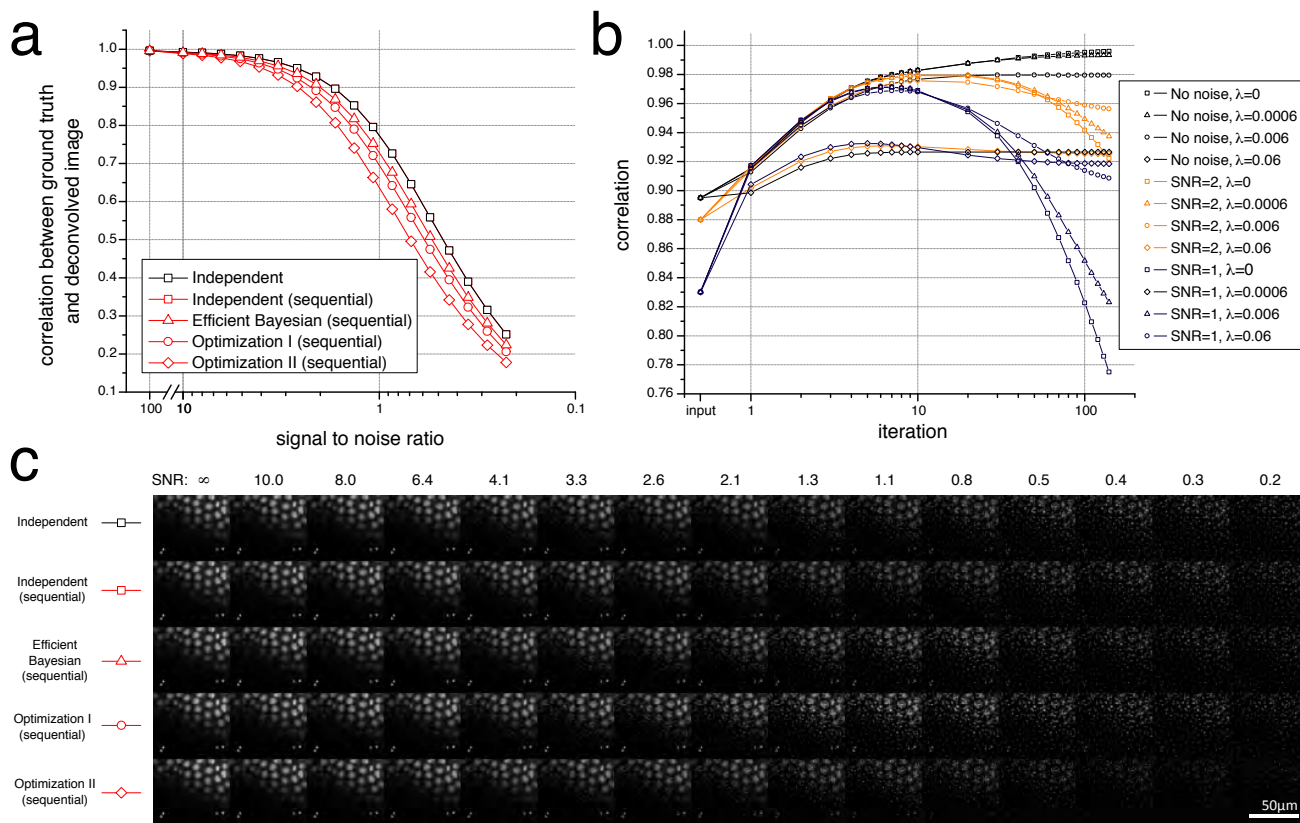
Supplementary Figure 4: *Performance comparison and dependence on the PSF* **(a)** The convergence time of the different algorithms until they reach the same average difference to the ground truth image shown in supplementary figure 5e. **(b)** The number of iterations required until all algorithms reach the same average difference to the ground truth image. One 'iteration' comprises all computational steps until each view contributed once to update the underlying distribution. **(c)** The total number of updates of the underlying distribution until the same average difference is reached. **(d)** The number of iterations required until the same difference to the ground truth is achieved using 4 views. The number of iterations is plotted relative to the angular difference between the input PSFs. An angular difference of 0 degrees refers to 4 identical PSFs and therefore 4 identical input images, an example of an angular difference of 45 degrees is shown in supplementary figure 5e. Plots are shown for different types of PSFs. **(a-d)** y-axis has logarithmic scale, all computations were performed on a dual-core Intel Core i7 with 2.7Ghz.

SUPPLEMENTARY FIGURE 5 — Images used for analysis and visual performance



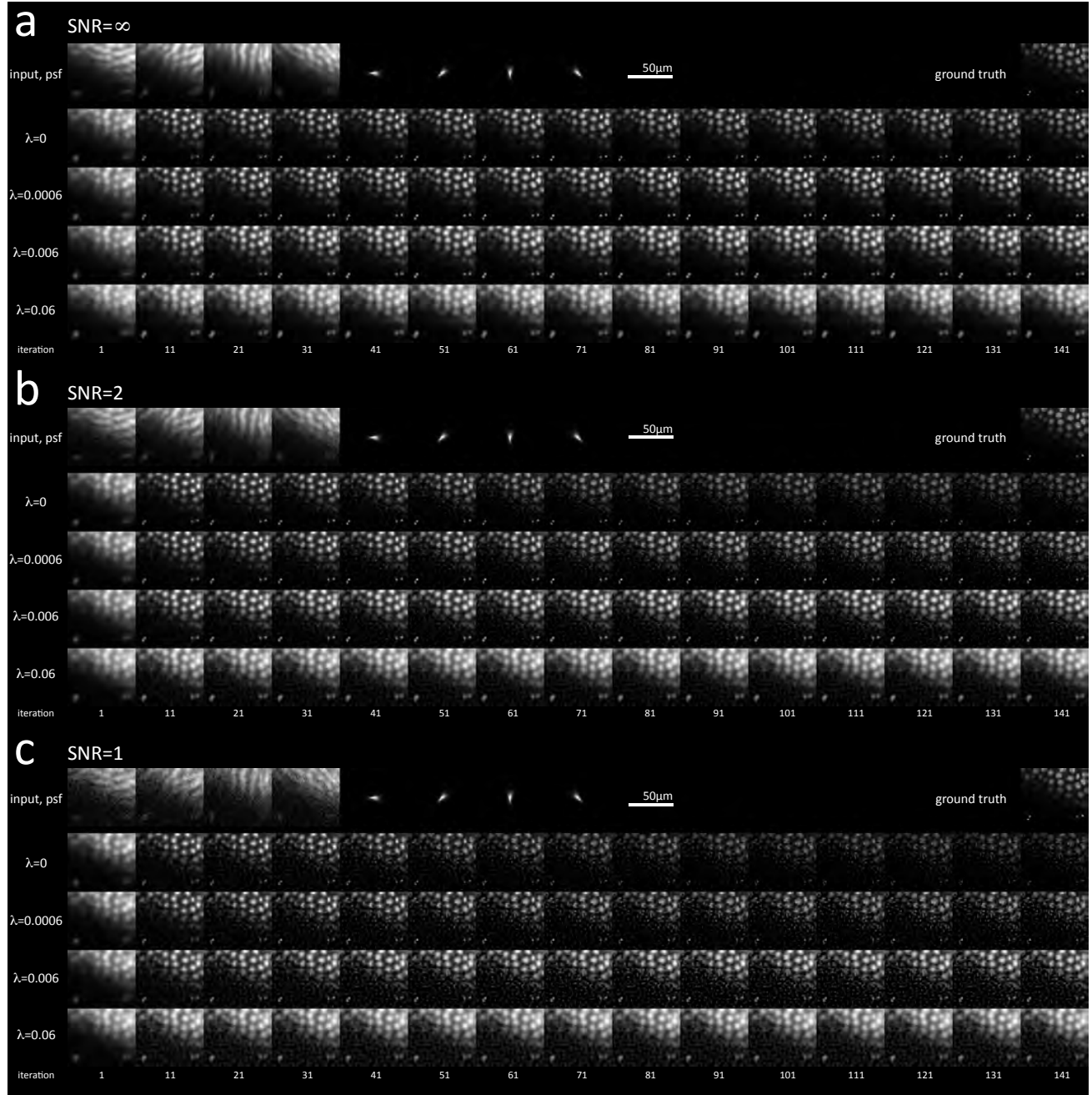
Supplementary Figure 5: *Images used for analysis and visual performance.* (a) The entire ground truth image used for all analyses shown in the supplement. (b) Reconstruction quality after 301 iterations using optimization II and sequential updates on 4 input views and PSF's as shown in (e). (c) Reconstruction quality after 14 iterations for the same input as (b). (d) Line-plot through the image highlighting the deconvolution quality after 301 (b) and 14 (c) iterations compared to the ground truth (a). (e) Magnification of a small region of the ground truth image (a), the 4 input PSF's and 4 input datasets as well as the results for all algorithms as used in supplementary figure 4a-c for performance measurements.

SUPPLEMENTARY FIGURE 6 — Effect of noise on the deconvolution results



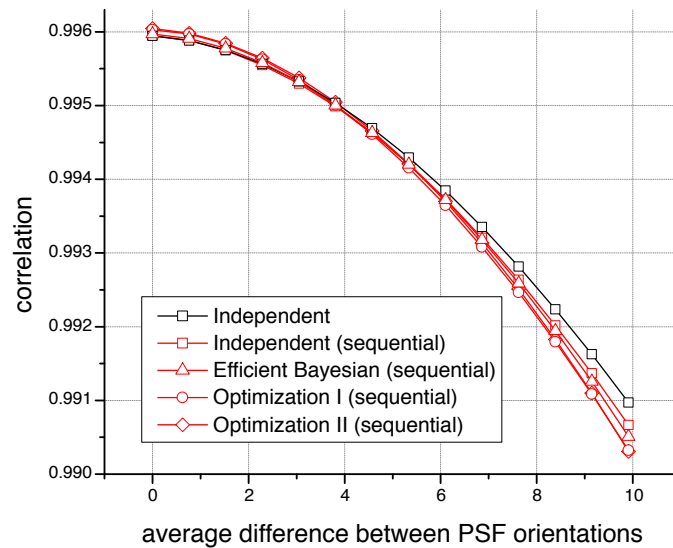
Supplementary Figure 6: *Effect of noise on the deconvolution results* (a) The resulting cross-correlation between the ground truth image and the deconvolved image depending on the signal-to-noise ratio in the input images. (b) The cross correlation between the ground truth image and the deconvolved image at certain iteration steps during the deconvolution shown for different signal-to-noise ratios (SNR= ∞ [no noise], SNR=2, SNR=1) and varying parameters of the Tikhonov regularization ($\lambda=0$ [no regularization], $\lambda=0.0006$, $\lambda=0.006$, $\lambda=0.06$). Supplementary figure 7 shows the corresponding images for all data points in this plot. This graph is based on the derivation assuming view independence using sequential updates in order to be able to illustrate the behaviour in early stages of the deconvolution. (c) Deconvolved images corresponding to the points in graph (a) to illustrate the resulting image quality from a certain correlation coefficient.

SUPPLEMENTARY FIGURE 7 — Intermediate stages of deconvolution results for varying SNR's and regularization



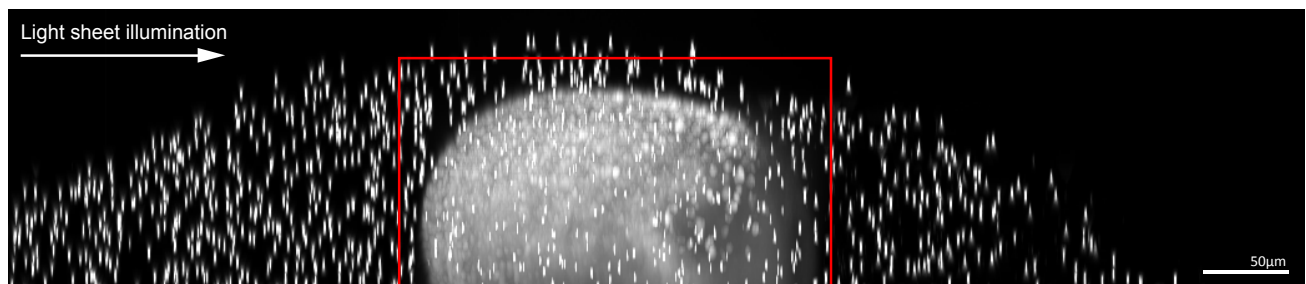
Supplementary Figure 7: *Intermediate stages of deconvolution results for varying SNR's and regularization.* (a-c) 1st row shows input data, PSF's and ground truth, 2nd–4th row the intermediate stages for varying parameters of the Tikhonov regularization ($\lambda=0$ [no regularization], $\lambda=0.0006$, $\lambda=0.006$, $\lambda=0.06$). All images refer to individual data points in supplementary figure 6b. (a) Deconvolution for SNR=∞ (no noise). Here, $\lambda=0$ shows best results. (b) Deconvolution for SNR=2. Small structures like the fluorescent beads close to each other remain separable. (c) Deconvolution for SNR=1. The fluorescent beads are not possible to tell apart in the input images any more. They remain separable at intermediate levels of Tikhonov regularization.

SUPPLEMENTARY FIGURE 8 — Quality of deconvolution for imprecise estimation of the PSF



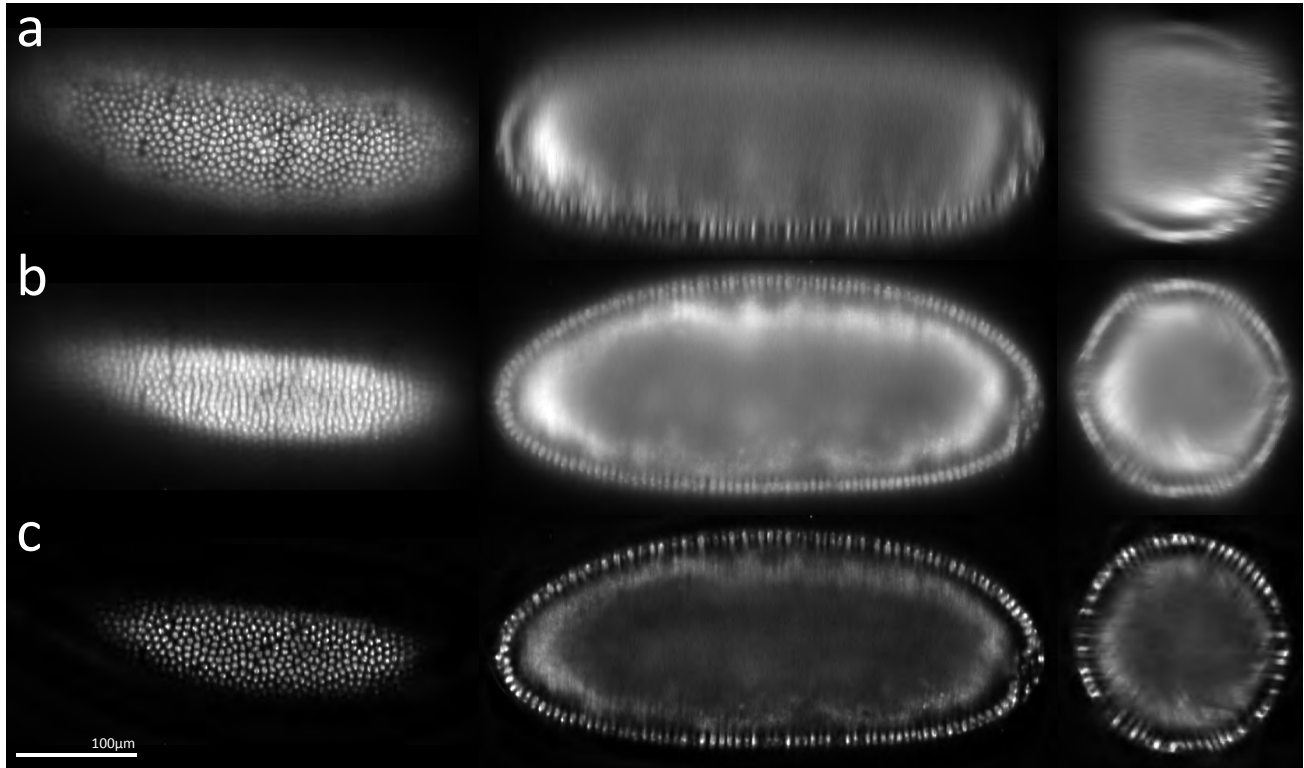
Supplementary Figure 8: *Quality of deconvolution for imprecise estimation of the PSF*. The cross-correlation between the deconvolved image and the ground truth images when the PSF's used for deconvolution were rotated by random angles relative to the PSF's used to create the input images.

SUPPLEMENTARY FIGURE 9 — Variation of the PSF across the light sheet in SPIM acquisitions



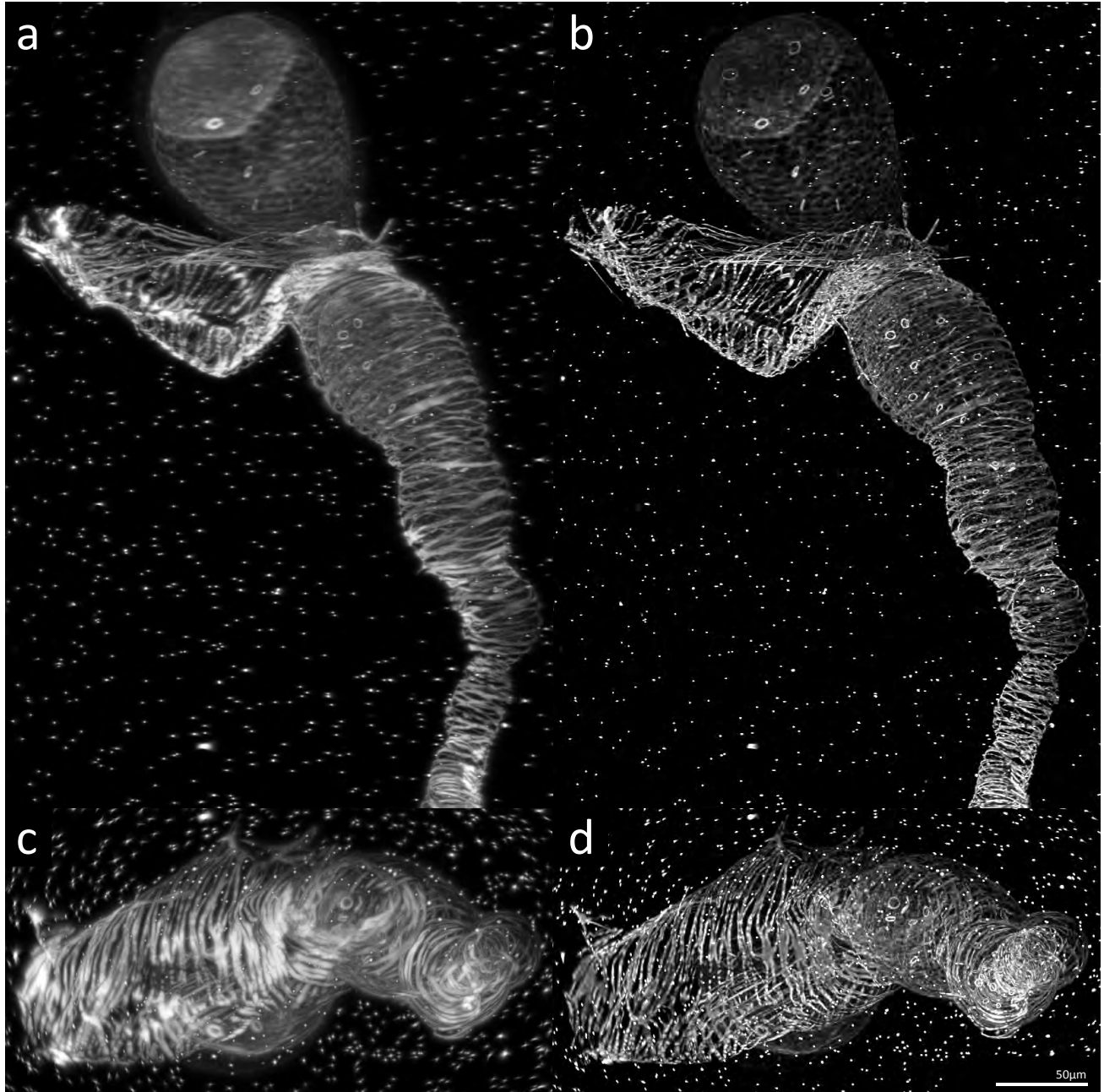
Supplementary Figure 9: *Variation of the PSF across the light sheet in SPIM acquisitions*. The maximum intensity projection perpendicular to the light sheet of a *Drosophila* embryo expressing His-YFP in all nuclei. The fluorescent beads have a diameter of 500nm. The arrow shows the illumination direction of the light sheet. The fluorescent beads should reflect the concave shape of a light sheet. The red box illustrates the area that is approximately used for deconvolution.

SUPPLEMENTARY FIGURE 10 — Quality of reconstruction for an OpenSPIM acquisition of *Drosophila* embryo



Supplementary Figure 10: *Comparison of reconstruction quality on the OpenSPIM.* (a) Quality of one of the input views as acquired by the OpenSPIM microscope. (b) Quality of the content-based fusion of the registered dataset. (c) Quality of the deconvolution of the registered dataset. (a-c) The first column shows a slice in the lateral orientation of the input dataset, the second column shows an orthogonal slice, the third column shows a slice perpendicular to the rotation axis. All slices are in the exactly same position and show the identical portion of each volume and are directly comparable. The light sheet thickness of the OpenSPIM is larger than of Zeiss prototype, therefore more out-of-focus light is visible and (a,b) are more blurred. Therefore the effect of deconvolution is especially visible, most dominantly in the third column showing the slice perpendicular to the rotation axis. The dataset has a size of $793 \times 384 \times 370$ px, acquired with in 6 views totalling around 680 million pixels and 2.6 gigabytes of data. Computation time for 12 iterations was 12 minutes on two Nvidia Quadro 4000 GPU's using optimization I.

SUPPLEMENTARY FIGURE 11 — Quality of reconstruction of Drosophila ovaries



Supplementary Figure 11: *Comparison of reconstruction quality of Drosophila ovaries acquired on the Zeiss SPIM prototype using maximum intensity projections.* (a) shows the content-based fusion along the orientation of one of the acquired views. (b) shows the same image deconvolved. (c) shows the projection along the rotation axis of the content-based fusion, (d) of the deconvolved dataset. The final dataset has a size of $822 \times 1211 \times 430$ px, acquired in 12 views totalling an input size of around 5 billion pixels and 19 gigabytes of data (32 bit floating point data required for deconvolution). Computation time for 12 iterations was 36 minutes on two Nvidia Quadro 4000 GPU's using optimization I.

SUPPLEMENTARY TABLES

SUPPLEMENTARY TABLE 1 — Summary of datasets used in this publication

Dataset	Dimensions	Computation Time, Iterations, Method	Machine
<i>Drosophila</i> embryo expressing His-YFP in all cells acquired with Zeiss SPIM prototype using a 20x/0.5 detection objective (Fig. 2c-e)*	720×380×350 px, 7 views	7 minutes, 12 iterations, optimization I, $\lambda = 0.006$	2× Nvidia Quadro 4000 [†] , 64 GB RAM
<i>Drosophila</i> embryo expressing His-YFP in all cells acquired with the Open-SPIM using a 20x/0.5 detection objective (Supp. Fig. 10)	793×384×370 px, 6 views	12 minutes [‡] , 12 iterations, optimization I, $\lambda = 0.006$	2× Nvidia Quadro 4000 [†] , 64 GB RAM
<i>Drosophila</i> ovaries acquired on the Zeiss SPIM prototype using a 20x/0.5 detection objective (Supp. Fig. 11)	1211×822×430 px, 12 views	36 minutes, 12 iterations, optimization I, $\lambda = 0.006$	2× Nvidia Quadro 4000 [†] , 64 GB RAM
<i>Drosophila</i> embryo expressing His-YFP in all cells acquired with Zeiss SPIM prototype using a 20x/0.5 detection objective (Supp. Video 2-4)	792×320×310 px, 6 views, 236 timepoints	24.3 hours, 12 iterations, optimization I, $\lambda = 0.006$	2× Nvidia Quadro 4000 [†] , 64 GB RAM
<i>Drosophila</i> embryo expressing Histone-H2Av-mRFPPruby fusion in all cells imaged on Zeiss Lightsheet Z1 with a 20x/1.0 detection objective and dual-sided illumination	928×390×390 px, 6 views, 715 timepoints	35 hours, 10 iterations, optimization I, $\lambda = 0.0006$	4× Nvidia TESLA [§] , 64 GB RAM
<i>C. elegans</i> embryo in 4-cell stage expressing PH-domain-GFP fusion acquired with Zeiss SPIM prototype using a 40x/0.8 detection objective (Fig. 2a,b)*	180×135×180 px, 6 views	1 minute, 20 iterations, optimization I, $\lambda = 0.006$	2× Intel Xeon E5-2630, 64 GB RAM
Fixed <i>C. elegans</i> larvae in L1 stage expressing LMN-1::GFP and stained with Hoechst imaged on Zeiss Lightsheet Z1 with a 20x/1.0 detection objective (Fig. 2f,g and Supp. Video 5-8)	1640×1070×345 px, 4 views, 2 channels	2×160 minutes, 100 iterations, optimization II, $\lambda = 0$	2× Intel Xeon E5-2690, 128 GB RAM

Supplementary Table 1: *Summary of all datasets used in this publication.* Note that the multi-view deconvolution of the *C. elegans* larvae in L1 stage required an additional registration step, which is explained in section 12.

*This SPIM acquisition was already used in Preibisch (2010)¹ to illustrate the results of the bead-based registration and multi-view fusion; we use the underlying dataset again to illustrate the improved results of the multi-view deconvolution.

[†]Two graphics cards in one PC, which can process two 512×512×512 blocks in parallel

[‡]Note that the increased computation time is due to larger anisotropy of the acquired stacks leading to larger effective PSF sizes, which increases the computational effort. The image could therefore not be split up into two 512×512×512 blocks as the other *Drosophila* datasets.

[§]Run on a cluster with 4 nodes that are equipped with one Nvidia TESLA and 64 GB of system memory

SUPPLEMENTARY NOTE

1. REMARKS

This document follows the notation introduced in the paper of L. B. Lucy² whenever possible. Note that for simplicity the derivations in this document only cover the one dimensional case. Nevertheless, all equations are valid for any n -dimensional case.

2. BAYESIAN SINGLE-VIEW DECONVOLUTION

This section re-derives the classical bayesian Richardson³-Lucy² deconvolution for single images, other derivations presented in this document build up on it. The goal is to estimate the frequency distribution of an underlying signal $\psi(\xi)$ from a finite number of measurements $x^{1'}, x^{2'}, \dots, x^{N'}$. The resulting observed distribution $\phi(x)$ is defined as

$$\phi(x) = \int_{\xi} \psi(\xi) P(x|\xi) d\xi \quad (1)$$

where $P(x|\xi)$ is the probability of a measurement occuring at $x = x'$ when it is known that the event $\xi = \xi'$ occurred. In more practical image analysis terms equation 1 describes the one-dimensional convolution operation where $\phi(x)$ is the blurred image, $P(x|\xi)$ is the kernel and $\psi(\xi)$ is the undegraded (or deconvolved) image. All distributions are treated as probability distributions and fulfill the following constraints:

$$\int_{\xi} \psi(\xi) d\xi = \int_x \phi(x) dx = \int_x P(x|\xi) dx = 1 \quad \text{and} \quad \psi(\xi) > 0, \phi(x) \geq 0, P(x|\xi) \geq 0 \quad (2)$$

2.1 Derivation of the iterative deconvolution scheme

The basis for the derivation of the bayesian deconvolution is the tautology

$$P(\xi = \xi' \wedge x = x') = P(x = x' \wedge \xi = \xi') \quad (3)$$

It states that it is equally probable that the event ξ' results in a measurement at x' and that the measurement at x' was caused by the event ξ' . Integrating equation 3 over the measured distribution yields

$$\int_x P(\xi \wedge x) dx = \int_x P(x \wedge \xi) dx \quad (4)$$

which can be expressed using conditional probabilities

$$\int_x P(\xi) P(x|\xi) dx = \int_x P(x) P(\xi|x) dx \quad (5)$$

which in correspondence to Lucy's notation looks like (equation 1)

$$\int_x \psi(\xi) P(x|\xi) dx = \int_x \phi(x) Q(\xi|x) dx \quad (6)$$

where $P(\xi) \equiv \psi(\xi)$, $P(x) \equiv \phi(x)$, $P(\xi|x) \equiv Q(\xi|x)$. $Q(\xi|x)$ denotes what Lucy calls the 'inverse' conditional probability to $P(x|\xi)$. It defines the probability that an event at ξ' occurred, given a specific measurement at x' . As $\psi(\xi)$ does not depend on x , equation 6 can be rewritten as

$$\psi(\xi) \overbrace{\int_x P(x|\xi) dx}^{=1} = \int_x \phi(x) Q(\xi|x) dx \quad (7)$$

hence (due to equation 2)

$$\psi(\xi) = \int_x \phi(x) Q(\xi|x) dx \quad (8)$$

which corresponds to the inverse of the convolution in equation 1. Although $Q(\xi|x)$ cannot be used to directly compute $\psi(\xi)$, *Bayes' Theorem* and subsequently equation 1 can be used to reformulate it as

$$Q(\xi|x) = \frac{\psi(\xi) P(x|\xi)}{\phi(x)} = \frac{\psi(\xi) P(x|\xi)}{\int_{\xi} \psi(\xi) P(x|\xi) d\xi} \quad (9)$$

Replacing $Q(\xi|x)$ in equation 8 yields

$$\psi(\xi) = \int_x \phi(x) \frac{\psi(\xi) P(x|\xi)}{\int_{\xi} \psi(\xi) P(x|\xi) d\xi} dx = \psi(\xi) \int_x \frac{\phi(x)}{\int_{\xi} \psi(\xi) P(x|\xi) d\xi} P(x|\xi) dx \quad (10)$$

which exactly re-states the deconvolution scheme introduced by Lucy and Richardson. As both sides of the equation contain the desired underlying (deconvolved) distribution $\psi(\xi)$, an iterative scheme is used to converge towards the correct solution

$$\psi^{r+1}(\xi) = \psi^r(\xi) \int_x \frac{\phi(x)}{\int_{\xi} \psi^r(\xi) P(x|\xi) d\xi} P(x|\xi) dx \quad (11)$$

where $\psi^0(\xi)$ is simply a constant distribution with each value being the average intensity of the measured distribution $\phi(x)$.

Equation 11 turns out to be a maximum-likelihood expectation maximization formulation,⁴ which works as follows. It computes pixel-by-pixel the quotient between the input image $\phi(x)$ and the convolution of the current guess of the deconvolved image $\psi^r(\xi)$ with the kernel (aka PSF) $P(x|\xi)$, which yields a per pixel difference. These values are initially large but will become very small upon convergence. This quotient image is subsequently convolved with the point spread function $P(x|\xi)$ reflecting which pixels influence each other. This also preserves smoothness. These resulting values are then pixel-wise multiplied with the current guess of the deconvolved image $\psi^r(\xi)$, yielding a new guess of the deconvolved image. Starting from an initial guess of an image with constant values, this scheme will converge towards the correct solution if the guess of the point spread function is correct and if the observed distribution is not degraded by noise, transformations, etc.

2.1.1 Integrating ξ and x

Note that convolution of $\psi^r(\xi)$ with $P(x|\xi)$ requires integration over ξ , while the convolution of the quotient image with $P(x|\xi)$ integrates over x . Integration over x can be formulated as convolution if $P(x|\xi)$ is constant by using inverted coordinates $P(-x|\xi)$. Note that it can be ignored if the kernel is symmetric $P(x|\xi) = P(-x|\xi)$. For single-view datasets this is often the case, whereas multi-view datasets typically have non-symmetric kernels due to their transformations resulting from image alignment.

3. BAYESIAN MULTI-VIEW DECONVOLUTION

This section shows for the first time the entire derivation of bayesian multi-view deconvolution using probability theory. Compared to the single-view case we have a set of views $V = \{v_1 \dots v_N : N = |V|\}$ comprising N observed distributions $\phi_v(x_v)$, N point spread functions $P_v(x_v|\xi)$ and one underlying signal distribution $\psi(\xi)$. The observed distributions $\phi_v(x_v)$ are accordingly defined as

$$\phi_1(x_1) = \int_{\xi} \psi(\xi) P(x_1|\xi) d\xi \quad (12)$$

$$\phi_2(x_2) = \int_{\xi} \psi(\xi) P(x_2|\xi) d\xi \quad (13)$$

$$\dots \quad (14)$$

$$\phi_N(x_N) = \int_{\xi} \psi(\xi) P(x_N|\xi) d\xi \quad (15)$$

The basis for the derivation of the bayesian multi-view deconvolution is again a tautology based on the individual observations

$$P(\xi = \xi' \wedge x_1 = x'_1 \wedge \dots \wedge x_N = x'_N) = P(x_1 = x'_1 \wedge \dots \wedge x_N = x'_N \wedge \xi = \xi') \quad (16)$$

Integrating equation 16 over the measured distributions yields

$$\int_{x_1} \dots \int_{x_N} P(\xi \wedge x_1 \wedge \dots \wedge x_N) dx_1 \dots dx_N = \int_{x_1} \dots \int_{x_N} P(x_1 \wedge \dots \wedge x_N \wedge \xi) dx_1 \dots dx_N \quad (17)$$

shortly written as

$$\int_{\bar{x}} P(\xi \wedge x_1 \wedge \dots \wedge x_N) d\bar{x} = \int_{\bar{x}} P(x_1 \wedge \dots \wedge x_N \wedge \xi) d\bar{x} \quad (18)$$

By expressing the term using conditional probabilities one obtains

$$\int_{\bar{x}} P(\xi) P(x_1|\xi) P(x_2|\xi, x_1) \dots P(x_N|\xi, x_1, \dots, x_{N-1}) d\bar{x} = \int_{\bar{x}} P(x_1) P(x_2|x_1) P(x_3|x_1, x_2) \dots P(x_N|x_1, \dots, x_{N-1}) P(\xi|x_1, \dots, x_N) d\bar{x} \quad (19)$$

On the left side of the equation all terms are conditionally independent of any x_v given ξ . This results from the fact that if an event $\xi = \xi'$ occurred, each individual measurement x_v depends only on ξ' and the respective point spread function $P(x_v|\xi)$ (supplementary figure 1a for illustration). Equation 19 therefore reduces to

$$P(\xi) \overbrace{\int_{\bar{x}} P(x_1|\xi) P(x_2|\xi) \dots P(x_N|\xi) d\bar{x}}^{=1} = \int_{\bar{x}} P(x_1) P(x_2|x_1) P(x_3|x_1, x_2) \dots P(x_N|x_1, \dots, x_{N-1}) P(\xi|x_1, \dots, x_N) d\bar{x} \quad (20)$$

Assuming independence of the observed distributions $P(x_v)$ equation 20 further simplifies to

$$P(\xi) = \int_{\bar{x}} P(x_1) P(x_2) P(x_3) \dots P(x_N) P(\xi|x_1, \dots, x_N) d\bar{x} \quad (21)$$

Although independence between the views is assumed,⁵⁻⁷ the underlying distribution $P(\xi)$ still depends on the observed distributions $P(x_v)$ through $P(\xi|x_1, \dots, x_N)$.

Note: In section 4 we will proof that that the formulation of bayesian multi-view deconvolution can be achieved without assuming independence of the observed distributions $P(x_v)$. Based on this proof we argue that there is some relationship between the $P(x_v)$'s (supplementary figure 1b for illustration). We will discuss the potential of incorporating it into the derivation in section 5 and 6.

We cannot approximate $P(\xi|x_1, \dots, x_N)$ directly and therefore need to reformulate it in order to express it using individual $P(\xi|x_v)$, which can subsequently be used to formulate the deconvolution task as shown in section 2. Note that according to Lucy's notation $P(\xi|x_1, \dots, x_N) \equiv Q(\xi|x_1, \dots, x_N)$ and $P(\xi|x_v) \equiv Q(\xi|x_v)$.

$$P(\xi|x_1, \dots, x_N) = \frac{P(\xi, x_1, \dots, x_N)}{P(x_1, \dots, x_N)} \quad (22)$$

$$P(\xi|x_1, \dots, x_N) = \frac{P(\xi) P(x_1|\xi) P(x_2|\xi, x_1) \dots P(x_N|\xi, x_1, \dots, x_{N-1})}{P(x_1) P(x_2|x_1) \dots P(x_N|x_1, \dots, x_{N-1})} \quad (23)$$

Due to the conditional independence of the $P(x_v)$ given ξ (equation 19 \rightarrow 20 and supplementary figure 1a) and the assumption of independence between the $P(x_v)$ (equation 20 \rightarrow 21) equation 23 simplifies to

$$P(\xi|x_1, \dots, x_N) = \frac{P(\xi) P(x_1|\xi) \dots P(x_N|\xi)}{P(x_1) \dots P(x_N)} \quad (24)$$

Using *Bayes' theorem* to replace all

$$P(x_v|\xi) = \frac{P(x_v) P(\xi|x_v)}{P(\xi)} \quad (25)$$

yields

$$P(\xi|x_1, \dots, x_N) = \frac{P(\xi) P(\xi|x_1)P(x_1)...P(\xi|x_N)P(x_N)}{P(x_1)...P(x_N) P(\xi)^N} \quad (26)$$

$$P(\xi|x_1, \dots, x_N) = \frac{P(\xi) P(\xi|x_1)...P(\xi|x_N)}{P(\xi)^N} \quad (27)$$

$$P(\xi|x_1, \dots, x_N) = \frac{P(\xi|x_1)...P(\xi|x_N)}{P(\xi)^{N-1}} \quad (28)$$

Substituting equation 28 in equation 21 yields

$$P(\xi) = \frac{\int_{\bar{x}} P(x_1) \dots P(x_N) P(\xi|x_1) \dots P(\xi|x_N) d\bar{x}}{P(\xi)^{N-1}} \quad (29)$$

and rewritten in Lucy's notation

$$\psi(\xi) = \frac{\int_{\bar{x}} \phi_1(x_1) \dots \phi_N(x_N) Q(\xi|x_1) \dots Q(\xi|x_N) d\bar{x}}{\psi(\xi)^{N-1}} \quad (30)$$

$$\psi(\xi) = \frac{\int_{x_1} \phi_1(x_1) Q(\xi|x_1) dx_1 \dots \int_{x_N} \phi_N(x_N) Q(\xi|x_N) dx_N}{\psi(\xi)^{N-1}} \quad (31)$$

$$\psi(\xi) = \frac{\prod_{v \in V} \int_{x_v} \phi_v(x_v) Q(\xi|x_v) dx_v}{\psi(\xi)^{N-1}} \quad (32)$$

As in the single view case we replace $Q(\xi|x_v)$ with equation 9

$$\psi(\xi) = \frac{\prod_{v \in V} \int_{x_v} \phi_v(x_v) \frac{\psi(\xi) P(x_v|\xi)}{\int_{\xi} \psi(\xi) P(x_v|\xi) d\xi} dx_v}{\psi(\xi)^{N-1}} \quad (33)$$

$$\psi(\xi) = \frac{\cancel{\psi(\xi)} \prod_{v \in V} \int_{x_v} \phi_v(x_v) \frac{P(x_v|\xi)}{\int_{\xi} \psi(\xi) P(x_v|\xi) d\xi} dx_v}{\cancel{\psi(\xi)^{N-1}}} \quad (34)$$

$$\psi(\xi) = \psi(\xi) \prod_{v \in V} \int_{x_v} \phi_v(x_v) \frac{P(x_v|\xi)}{\int_{\xi} \psi(\xi) P(x_v|\xi) d\xi} dx_v \quad (35)$$

As in the single view case, both sides of the equation contain the desired deconvolved distribution $\psi(\xi)$. This again suggests the final iterative scheme

$$\psi^{r+1}(\xi) = \psi^r(\xi) \prod_{v \in V} \int_{x_v} \frac{\phi_v(x_v)}{\int_{\xi} \psi^r(\xi) P(x_v|\xi) d\xi} P(x_v|\xi) dx_v \quad (36)$$

where $\psi^0(\xi)$ is considered a distribution with a constant value. Note that the final derived equation 36 ends up being the per pixel multiplication of the single view deconvolution from equation 11.

3.1 EXPRESSION IN CONVOLUTION ALGEBRA

In order to be able to efficiently compute equation 36 the integrals need to be expressed as convolutions, which can be computed in *Fourier Space* using the *Convolution Theorem*. Expressing equation 36 in convolution

algebra (see also equation 1) requires two assumptions. Firstly, we assume the point spread functions $P(x_v|\xi)$ to be constant for every location in space. Secondly, we assume that the different coordinate systems ξ and $x_1 \dots x_N$ are identical, i.e. they are related by an identity transformation. We can assume that, as prior to the deconvolution the datasets have been aligned using the bead-based registration algorithm.¹ The reformulation yields

$$\psi^{r+1} = \psi^r \prod_{v \in V} \frac{\phi_v}{\psi^r * P_v} * P_v^* \quad (37)$$

where $*$ refers to the convolution operator, \cdot and \prod to scalar multiplication, $-$ to scalar division and

$$P_v \equiv P(x_v|\xi) \quad (38)$$

$$\phi_v \equiv \phi_v(x_v) \quad (39)$$

$$\psi^r \equiv \psi^r(\xi) \quad (40)$$

Note that P_v^* refers to the mirrored version of kernel P_v (see section 2.1.1 for the explanation).

4. PROOF OF CORRECTNESS OF ASSUMING INDEPENDENCE OF THE VIEWS

Previous derivations of the bayesian multi-view deconvolution⁵⁻⁷ assumed independence of the individual views in order to derive variants of equation 36. The following derivation proofs that it is actually not necessary to assume independence of the observed distributions $\phi_v(x_v)$ (equation 20 \rightarrow 21 and equation 23 \rightarrow 24) in order to derive the formulation for bayesian multi-view deconvolution shown in equation 36. We therefore rewrite equation 21 without assuming independence (which is then identical to equation 20) and obtain

$$P(\xi) = \int_{\bar{x}} P(x_1)P(x_2|x_1) \dots P(x_N|x_1, \dots, x_{N-1})P(\xi|x_1, \dots, x_N)d\bar{x} \quad (41)$$

We consequently also do not assume independence in equation 24, which intends to replace $P(\xi|x_1, \dots, x_N)$, and obtain

$$P(\xi|x_1, \dots, x_N) = \frac{P(\xi)P(x_1|\xi) \dots P(x_N|\xi)}{P(x_1)P(x_2|x_1) \dots P(x_N|x_1, \dots, x_{N-1})} \quad (42)$$

Replacing equation 42 in 41 yields

$$P(\xi) = \int_{\bar{x}} P(x_1)P(x_2|x_1) \dots P(x_N|x_1, \dots, x_{N-1}) \frac{P(\xi)P(x_1|\xi) \dots P(x_N|\xi)}{P(x_1)P(x_2|x_1) \dots P(x_N|x_1, \dots, x_{N-1})} d\bar{x} \quad (43)$$

Cancelling out all terms below the fraction bar (from equation 42) with the terms in front of the fraction bar (from equation 41) results in

$$P(\xi) = \int_{\bar{x}} P(\xi)P(x_1|\xi) \dots P(x_N|\xi)d\bar{x} \quad (44)$$

Using again *Bayes' theorem* to replace all

$$P(x_v|\xi) = \frac{P(x_v)P(\xi|x_v)}{P(\xi)} \quad (45)$$

yields

$$P(\xi) = \frac{\int_{\bar{x}} P(\xi)P(x_1)P(\xi|x_1) \dots P(x_N)P(\xi|x_N)d\bar{x}}{P(\xi)^N} \quad (46)$$

$$P(\xi) = \frac{\int_{\bar{x}} P(x_1) \dots P(x_N)P(\xi|x_1) \dots P(\xi|x_N)d\bar{x}}{P(\xi)^{N-1}} \quad (47)$$

which is identical to equation 29. This proves that we can derive the final equation 36 without assuming independence of the observed distributions.

*Note: Despite the fact that we show in this section that equation 36 can be derived without assuming independence of the views, we will refer to this derivation as being based on **view independence** throughout the document in order to refer to it unambiguously.*

5. EFFICIENT BAYESIAN MULTI-VIEW DECONVOLUTION

Section 4 proves that the derivation of bayesian multi-view deconvolution does not require the assumption that the observed distributions (views) are independent. We want to take advantage of that and incorporate the relationship between them into the deconvolution process to reduce convergence time. In order to express these dependencies we need to understand and model the conditional probabilities $P(x_w|x_v)$ describing how one view $\phi_w(x_w)$ depends on another view $\phi_v(x_v)$.

5.1 MODELING CONDITIONAL PROBABILITIES

Let us assume that we made an observation $x_v = x'_v$ (see also supplementary figure 1b). The 'inverse' point spread function $Q(\xi|x_v)$ defines a probability for each location of the underlying distribution that it caused the event $\xi = \xi'$ that lead to this observation. Based on this probability distribution, the point spread function of any other observation $P(x_w|\xi)$ can be used to consecutively assign a probability to every of its locations defining how probable it is to expect an observation $x_w = x'_w$ corresponding to $x_v = x'_v$. Assuming the point spread function $P(x_w|\xi)$ is known, this illustrates that we are able to estimate the conditional probability $P(x_w|x_v = x'_v)$ for every location $x_w = x'_w$ as well as we can estimate the 'inverse' point spread function $Q(\xi|x_v)$.

However, we want to be able to compute an entire 'virtual' distribution, which is based on not only one singular event $x_v = x'_v$, but an entire observed distribution $\phi_v(x_v)$. Such a 'virtual' distribution is solely based on the conditional probabilities $P(x_w|x_v)$ and summarizes our knowledge about a distribution $\phi_w(x_w)$ by just observing $\phi_v(x_v)$ and knowing the (inverse) point spread functions $Q(\xi|x_v)$ and $P(x_w|\xi)$. We denote a 'virtual' distribution $\phi_v^V(x_w)$; the subscript v denotes the observed distribution it is based on, w defines the distribution that is estimated and V labels it as 'virtual' distribution.

The derivation of the formulation for a 'virtual' distribution is based on equations 1 and 8. The 'inverse' point spread function $Q(\xi|x_v)$ relates $\phi_v(x_v)$ to the underlying signal distribution $\psi(\xi)$, and the point spread function $P(x_w|\xi)$ consecutively relates it to the conditionally dependent signal distribution $\phi_w(x_w)$ (see also supplementary figure 1b)

$$\psi(\xi) = \int_{x_v} \phi_v(x_v) Q(\xi|x_v) dx_v \quad (48)$$

$$\phi_w(x_w) = \int_{\xi} \psi(\xi) P(x_w|\xi) d\xi \quad (49)$$

Substituting equation 48 in equation 49 yields

$$\phi_w(x_w) = \int_{\xi} \int_{x_v} \phi_v(x_v) Q(\xi|x_v) dx_v P(x_w|\xi) d\xi \quad (50)$$

As discussed in sections 2 and 3, we cannot use $Q(\xi|x_v)$ directly to compute $\psi(\xi)$. Using *Bayes' theorem* it can be rewritten as

$$Q(\xi|x_v) = \frac{\psi(\xi) P(x_v|\xi)}{\phi_v(x_v)} \quad (51)$$

Assuming $\phi_v(x_v)$ and $\psi(\xi)$ constant (or rather identical) simplifies equation 51 to

$$Q(\xi|x_v) \approx P(x_v|\xi) \quad (52)$$

This assumption reflects that initially we do not have any prior knowledge of $Q(\xi|x_v)$ and therefore need to set it equal to the PSF $P(x_v|\xi)$, which states the worst-case scenario. In other words, the PSF constitutes an upper bound of all the possible locations of the underlying distribution $\psi(\xi)$ that could contribute to the observed distribution given an observation at a specific location $x_v = x'_v$. Thus, this assumption renders the estimate $\phi_v^{V_w}(x_w)$ less precise (equation 53 and supplementary figure 2), while not omitting any of the possible solutions. Note that it would be possible to improve the guess of $Q(\xi|x_v)$ after every iteration. However, it would require a convolution with a different PSF at every location, which is currently computationally not feasible and therefore omitted. Replacing equation 52 in equation 50 yields

$$\phi_w(x_w) \approx \phi_v^{V_w}(x_w) = \int_{\xi} \int_{x_v} \phi_v(x_v) P(x_v|\xi) dx_v P(x_w|\xi) d\xi \quad (53)$$

Equation 53 enables the estimation of entire 'virtual' distributions $\phi_v^{V_w}(x_w)$, see supplementary figure 2 for a visualization. These 'virtual' distributions constitute an upper boundary describing how a distribution $\phi_w(x_w) \approx \phi_v^{V_w}(x_w)$ could look like while only knowing $\phi_v(x_v)$ and the two PSF's $P(x_v|\xi)$ and $P(x_w|\xi)$.

5.2 INCORPORATING VIRTUAL VIEWS INTO THE DECONVOLUTION SCHEME

In order to incorporate this knowledge into the deconvolution process (equation 36), we perform updates not only based on the observed distributions $\phi_v(x_v)$ but also all possible virtual distributions $\phi_v^{V_w}(x_w)$ as modelled by equation 53 and shown in supplementary figure 2. Based on all observed distributions

$$V = \{\phi_1(x_1), \phi_2(x_2), \dots, \phi_N(x_N)\} \quad (54)$$

we can estimate the following 'virtual' distributions

$$W = \{\phi_1^{V_2}(x_2), \phi_1^{V_3}(x_3), \dots, \phi_1^{V_N}(x_N), \phi_2^{V_1}(x_1), \phi_2^{V_3}(x_3), \dots, \phi_2^{V_N}(x_N), \dots, \phi_N^{V_{N-1}}(x_{N-1})\} \quad (55)$$

where

$$|W| = (N-1)^N : N = |V| \quad (56)$$

Note that if only one input view exists, $W = \emptyset$. We define subsets $W_v \subseteq W$, which depend on specific observed distributions $\phi_v(x_v)$ as follows

$$W_1 = \{\phi_1^{V_2}(x_2), \phi_1^{V_3}(x_3), \dots, \phi_1^{V_N}(x_N)\} \quad (57)$$

$$W_2 = \{\phi_2^{V_1}(x_1), \phi_2^{V_3}(x_3), \dots, \phi_2^{V_N}(x_N)\} \quad (58)$$

$$\dots \quad (59)$$

$$W_N = \{\phi_N^{V_1}(x_1), \phi_N^{V_2}(x_2), \dots, \phi_N^{V_{N-1}}(x_{N-1})\} \quad (60)$$

where

$$W = \bigcup_{v \in V} W_v \quad (61)$$

Incorporating the virtual distributions into the multi-view deconvolution (equation 36) yields

$$\psi^{r+1}(\xi) = \psi^r(\xi) \prod_{v \in V} \int_{x_v} \frac{\phi_v(x_v)}{\int_{\xi} \psi^r(\xi) P(x_v|\xi) d\xi} P(x_v|\xi) dx_v \prod_{w \in W_v} \int_{x_w} \frac{\phi_v^{V_w}(x_w)}{\int_{\xi} \psi^r(\xi) P(x_w|\xi) d\xi} P(x_w|\xi) dx_w \quad (62)$$

This formulation is simply a combination of observed and 'virtual' distributions, which does not yield any advantages in terms of computational complexity yet. During the following steps we will show that using a single assumption we are able to combine the update steps of the observed and 'virtual' distributions into one single update step for each observed distribution.

For simplicity we focus on one observed distribution $\phi_v(x_v)$ and its corresponding subset of 'virtual' distributions W_v . Note that the following assumptions and simplifications apply to all subsets individually.

$$\int_{x_v} \frac{\phi_v(x_v)}{\int_{\xi} \psi^r(\xi) P(x_v|\xi) d\xi} P(x_v|\xi) dx_v \prod_{w \in W_v} \int_{x_w} \frac{\phi_v^w(x_w)}{\int_{\xi} \psi^r(\xi) P(x_w|\xi) d\xi} P(x_w|\xi) dx_w \quad (63)$$

First, the 'virtual' distributions $\phi_v^w(x_w)$ are replaced with equation 53 which yields

$$\int_{x_v} \frac{\phi_v(x_v)}{\int_{\xi} \psi^r(\xi) P(x_v|\xi) d\xi} P(x_v|\xi) dx_v \prod_{w \in W_v} \int_{x_w} \frac{\int_{\xi} \int_{x_v} \phi_v(x_v) P(x_v|\xi) dx_v P(x_w|\xi) d\xi}{\int_{\xi} \psi^r(\xi) P(x_w|\xi) d\xi} P(x_w|\xi) dx_w \quad (64)$$

Note that $\int_{\xi} \psi^r(\xi) P(x_w|\xi) d\xi$ corresponds to our current guess of the observed distribution $\phi_w(x_w)$, which is based on the current guess of the underlying distribution $\psi^r(\xi)$ and the point spread function $P(x_w|\xi)$ (equation 1). In order to transform it into a 'virtually' observed distribution compatible with $\phi_v^w(x_w)$, we also apply equation 53, i.e. we compute it from the current guess of the observed distribution $\phi_v(x_v)$ yielding

$$\int_{x_v} \frac{\phi_v(x_v)}{\int_{\xi} \psi^r(\xi) P(x_v|\xi) d\xi} P(x_v|\xi) dx_v \prod_{w \in W_v} \int_{x_w} \frac{\int_{\xi} \int_{x_v} \phi_v(x_v) P(x_v|\xi) dx_v P(x_w|\xi) d\xi}{\int_{\xi} \int_{x_v} \int_{\xi} \psi^r(\xi) P(x_v|\xi) d\xi P(x_v|\xi) dx_v P(x_w|\xi) d\xi} P(x_w|\xi) dx_w \quad (65)$$

To better illustrate the final simplifications we transform equation 65 into convolution algebra (section 3.1). The reformulation yields

$$\frac{\phi_v}{\psi^r * P_v} * P_v^* \prod_{w \in W_v} \frac{\phi_v * \overbrace{P_v^* * P_w}^{\text{equation 53}}}{\psi^r * P_v * \underbrace{P_v^* * P_w}_{\text{equation 53}}} * P_w^* \quad (66)$$

Additional simplification of equation 66 requires an assumption in convolution algebra that we incorporate twice. Given three functions f , g and h we assume

$$(f * g) \cdot (f * h) \approx f * (g \cdot h) \quad (67)$$

We show in supplementary figure 3 that for *Gaussian*-like distributions this assumption approximately holds true after normalization of both sides of the equation. Note that the measured PSF's usually resemble a distribution similar to a gaussian (supplementary figure 5 and 9).

The numerator and the denominator of the ratio of the 'virtual' distribution in equation 66 both contain two consecutive convolutions with P_v^* and P_w as indicated by brackets. Based on equation 67 we assume

$$\frac{(g * f)}{(h * f)} \approx \left(\frac{g}{h}\right) * f \quad (68)$$

where

$$f \equiv P_v^* * P_w \quad (69)$$

$$g \equiv \phi_v \quad (70)$$

$$h \equiv \psi^r * P_v \quad (71)$$

and

$$\frac{(g * f)}{(h * f)} = (g * f) \cdot \frac{1}{(h * f)} = (g * f) \cdot \left(\frac{1}{h} * f\right) = \overbrace{(f * g) \cdot \left(f * \frac{1}{h}\right)}^{\text{equation 67}} \approx f * \left(g \cdot \frac{1}{h}\right) = f * \left(\frac{g}{h}\right) = \left(\frac{g}{h}\right) * f \quad (72)$$

Based on this assumption we can rewrite equation 66 as

$$\frac{\phi_v}{\psi^r * P_v} * P_v^* \prod_{w \in W_v} \frac{\phi_v}{\psi^r * P_v} * \overbrace{P_v^* * P_w * P_w^*}^{\text{equation 53}} \quad (73)$$

Note that this reformulation yields two identical terms as outlined by brackets describing the ratio between the observed distribution ϕ_v and its guess based on the current iteration of the deconvolved distribution $\psi^r * P_v$. To further simplify equation 73 we apply the assumption (equation 67) again where

$$f \equiv \frac{\phi_v}{\psi^r * P_v} \quad (74)$$

$$g \equiv P_v^* \quad (75)$$

$$h \equiv P_v^* * P_w * P_w^* \quad (76)$$

which yields

$$\frac{\phi_v}{\psi^r * P_v} * \left(P_v^* \prod_{w \in W_v} P_v^* * P_w * P_w^* \right) \quad (77)$$

In the context of all observed distributions, the final formula for efficient bayesian multi-view deconvolution reads

$$\psi^{r+1} = \psi^r \prod_{v \in V} \frac{\phi_v}{\psi^r * P_v} * \overbrace{\left(P_v^* \prod_{w \in W_v} P_v^* * P_w * P_w^* \right)}^{P_v^{compound}} \quad (78)$$

Equation 78 incorporates all observed and 'virtual' distributions that speed up convergence, but requires the exactly same number of computations as the normal multi-view deconvolution (equation 36) derived in section 3. The only additional computational overhead is the initial computation of the *compound* kernels for each observed distribution

$$P_v^{compound} = P_v^* \prod_{w \in W_v} \overbrace{P_v^* * P_w * P_w^*}^{P_{w_v}^{compound}} \quad (79)$$

The compound kernel for a specific observed distribution ϕ_v is computed by scalar multiplication of its mirrored point spread function P_v^* with all 'virtual' compound kernels $P_{w_v}^{compound}$ based on the corresponding 'virtual' distributions $\phi_v^{V_w}(x_w) \in W_v$. All individual 'virtual' compound kernels are computed by convolving P_v^* with P_w and sequentially with P_w^* . For most multi-view deconvolution scenarios the computational effort for the pre-computation of the compound kernels can be neglected as the PSF's are very small compared to the images and they need to be computed only once.

6. AD-HOC OPTIMIZATIONS OF THE EFFICIENT BAYESIAN MULTI-VIEW DECONVOLUTION

The efficient bayesian multi-view deconvolution derived in section 5 offers possibilities for optimizations as the assumption underlying the estimation of the conditional probabilities (section 5.1) results in smoothed guess of the 'virtual' distributions (supplementary figure 2c). Therefore, the core idea underlying all subsequently presented alterations of equation 78 is to change how the 'virtual' distributions are computed. Due to the optimizations introduced in the last section, this translates to modification of the 'virtual' compound kernels

$$P_{w_v}^{compound} = P_v^* * P_w * P_w^* \quad (80)$$

The goal is to decrease convergence time while preserving reasonable deconvolution results. This can be achieved by sharpening the 'virtual' distribution (supplementary figure 2c) without omitting possible solutions or rendering them too unlikely.

6.1 OPTIMIZATION I - REDUCED DEPENDENCE ON VIRTUALIZED VIEW

The computation of the 'virtual' compound kernels contains two convolutions with the point spread function of the 'virtualized' observation, one with P_w and one with P_w^* . We found that skipping the convolution with P_w^* significantly reduces convergence time while producing almost identical results even in the presence of noise (section 8 and 9).

$$\psi^{r+1} = \psi^r \prod_{v \in V} \frac{\phi_v}{\psi^r * P_v} * \left(P_v^* \prod_{w \in W_v} P_v^* * P_w \right) \quad (81)$$

6.2 OPTIMIZATION II - NO DEPENDENCE ON VIRTUALIZED VIEW

We determined empirically that further assuming P_w to be constant still produces reasonable results while further reducing convergence time. We are aware that this is quite an ad-hoc assumption, but in the presence of low noise levels still yields adequate results (section 8 and 9).

$$\psi^{r+1} = \psi^r \prod_{v \in V} \frac{\phi_v}{\psi^r * P_v} * \prod_{v, w \in W_v} P_v^* \quad (82)$$

Interestingly, this formulation shows similarity to an optimization of the classic single-view Richardson-Lucy deconvolution which incorporates an exponent into the 'correction factor'.⁸

6.3 NO DEPENDENCE ON OBSERVED VIEW

Only keeping the convolutions of the 'virtualized' observation, i.e. P_w and P_w^* yields a non-functional formulation. This is in agreement with the estimation of the conditional probabilities (section 5.1).

7. ALTERNATIVE ITERATION FOR FASTER CONVERGENCE

To further optimize convergence time we investigated the equations 36 and 78 in detail. Both multi-view deconvolution formulas evaluate all views in order to compute one single update step of $\psi(\xi)$. It was already noted that in both cases each update step is simply the multiplication of all contributions from each observed distribution. This suggests an alternative update scheme where the individual contributions from each observed distribution are directly used to update $\psi(\xi)$ in order to save computation time. In this iteration scheme, equation 78 reads as follows

$$\psi^{r+1} = \psi^r \frac{\phi_1}{\psi^r * P_1} * \left(P_1^* \prod_{w \in W_1} P_1^* * P_w * P_w^* \right) \quad (83)$$

$$\psi^{r+2} = \psi^{r+1} \frac{\phi_2}{\psi^{r+1} * P_2} * \left(P_2^* \prod_{w \in W_2} P_2^* * P_w * P_w^* \right) \quad (84)$$

$$\dots \quad (85)$$

$$\psi^{r+N} = \psi^{r+N-1} \frac{\phi_N}{\psi^{r+N-1} * P_N} * \left(P_N^* \prod_{w \in W_N} P_N^* * P_w * P_w^* \right) \quad (86)$$

$$(87)$$

Note that for equation 36 (equation 37) the iterative scheme looks identical when the multiplicative part of the compound kernel is left out; it actually corresponds to the sequential application of the bayesian single view deconvolution (equation 11).

8. BENCHMARKS

We compare the performance of the efficient bayesian multi-view deconvolution (section 5, equation 78) and its optimizations I & II (sections 6.1 and 6.2, equations 81 and 82) against the derivation based on view independence (sections 3 and 4, equations 36 and 37) for combined (sections 3 – 6) and sequential (section 7) updates of the underlying distribution using ground truth images. The iteration behaviour of the deconvolution depends on the image contents and the shape of the PSF (supplementary figure 4d). In order to make the simulations relatively realistic for microscopic multi-view acquisitions, we chose as ground truth image one plane of a SPIM acquisition of a *Drosophila* embryo expressing His-YFP in all cells (supplementary figure 5a,e) that we blur with a maximum intensity projection of a PSF in axial direction (xz), extracted from an actual SPIM acquisition (supplementary figure 5e).

8.1 CONVERGENCE TIME, NUMBER OF ITERATIONS & UPDATES

Supplementary figure 4a-c illustrate computation time, number of iterations and number of updates of the underlying distribution that are required by the different derivations to converge to a point, where they achieve exactly the same average difference between the deconvolved image and the ground truth. Detailed parts of the ground truth, PSFs, input images and results used for supplementary figure 4 are exemplarily pictured for 4 views in supplementary figure 5e, illustrating that all algorithms actually converge to the same result. The entire ground truth picture is shown in supplementary figure 5a, the deconvolution result as achieved in the benchmarks is shown in supplementary figure 5b.

Supplementary figure 4a shows that our new derivation taking into account conditional probabilities (equation 78) outperforms the derivation that is based on view independence (equation 36) by a factor of around 1.5–2.5, depending on the number of views involved. Optimization I is faster by a factor of 2–4, optimization II by a factor of 3–8. Sequential updates pictured in red additionally speed up the computation by a factor of approximately n , where n describes the number of views involved. This additional multiplicative speed-up is independent of the derivation used. Note the logarithmic scale of all y-axes in supplementary figure 4.

It is striking that for combined updates (black) the computation time first decreases, but quickly starts to increase with the number of views involved. In contrast, for sequential updates the computation time decreases and then plateaus. The increase in computation time becomes clear when investigating the required number of iterations[¶] (supplementary figure 4b). The number of iteration for combined updates (black) almost plateaus at a certain level, however, with increasing number of views, the computational effort to compute one update increases linearly. This leads to an almost linear increase in convergence time with an increasing number of views when using combined updates. When using sequential updates (red), the underlying distribution is updated for each view individually, hence the number of required iterations continuously decreases and only the convergence time plateaus with an increasing number of views. Supplementary figure 4c supports this interpretation by illustrating that for each derivation the number of updates of the underlying distribution defines when the same quality of deconvolution is achieved.

In any case, having more than one view available for the deconvolution process decreases computation time and number of required updates significantly. This effect is especially prominent at a low number of views. For example adding a second view decreases the computation time in average 45-fold, a third view still on average another 1.5-fold.

One can argue that using combined update steps allows better parallelization of the code as all view contributions can be computed at the same time, whereas sequential updating requires to compute one view after the other. In practice, computing the update step for an individual view is already almost perfectly multi-threadable. It requires of two convolutions computed in Fourier space and several per-pixel operations. Even when several

[¶]Note that we consider one iteration completed when all views contributed to update the underlying distribution once. In the case of combined updates this refers to one update of the underlying distribution, in case of sequential updates this refers to n updates.

GPU's are available it can be parallelized as it can be split into blocks. Using sequential updates additionally offers the advantage that the memory required for the computation is significantly reduced.

8.1.1 VISUAL IMAGE QUALITY

Supplementary figure 5c shows the result using optimization II and sequential updates after 14 iterations, the same quality as achieved by all algorithms as shown in supplementary figure 5e and used for the benchmarks in supplementary figure 4. In this case the quality of the deconvolved image is sufficient to separate small details like the fluorescent beads, which is not possible in the input images (supplementary figure 5e, right top). 301 iterations almost perfectly restore the image (supplementary figure 5b,d). In comparison, the derivation based on view independence (equation 36) and combined updates needs 301 iteration to simply arrive at the quality pictured in supplementary figure 5c,e.

8.2 GENERAL DEPENDENCE ON THE PSF's

For supplementary figure 4a-c the PSF's are arranged in a way so that the angular difference between them is maximal in the range from 0–180 degrees (supplementary figure 5e). Supplementary figure 4d visualizes for 4 views that the angular difference between the views significantly influences the convergence behaviour. Looking at two extreme cases explains this behaviour. In this synthetic environment a difference of 0 degrees between PSF's corresponds to 4 identical PSF's and therefore 4 identical input images. This constellation is identical to having just one view, which results in a very long convergence time (supplementary figure 4a). The same almost applies for 180 degrees as the PSF that was used is quite symmetrical. In those extreme cases our argument that we can learn something about a second view by looking at the first view (section 5.1) does not hold. Therefore our derivation taking into account conditional probabilities as well as the optimizations do not converge to the identical result and few datapoints close and equal to 0 and 180 degrees are omitted. Note that they still achieve a reasonable result, but simply cannot be plotted as this quality of reconstruction is not achieved.

In general, convergence time decreases as the level of overlap between the PSFs decreases. In case of non-isotropic, gaussian-like PSFs rotated around the center (as in multi-view microscopy), this translates to a decrease in convergence time with an increase in angular difference. From this we can derive that for overlapping multi-view acquisitions it should be advantageous to prefer an odd over an even number of equally spaced views.

Supplementary figure 4d also illustrates that convergence time significantly depends on the shape and size of the PSF. Different PSF's require different amount of iterations until they reach the same quality. Intuitively this has to be true, as for example the most simple PSF consisting only of its central pixel does not require any deconvolution at all. Conversely, this also holds true for the images themselves; the iteration time required to reach a certain quality depends on the content. For example, the synthetic image used in Supplementary Movie 1 takes orders of magnitude longer to converge to same cross correlation of 0.99 to ground truth, compared to the image in supplementary figure 5a using the same PSF's, algorithm and iteration scheme.

9. NOISE AND REGULARIZATION

Although noise is typically quite low in light-sheet microscopy^{||}, it is a common problem and we therefore investigated the effect of noise on the performance of the different algorithms. We added incremental amounts of gaussian noise to the input data, which was used as input for the deconvolution to estimate the effects. The first rows in supplementary figure 7a-c illustrate the quality of the input images for 3 different signal-to-noise (SNR) levels.

A comparison as in the previous section is unfortunately not possible as in the presence of noise none of the algorithms converges exactly towards the ground truth. Note that still very reasonable results are achieved

^{||}In our images the lowest SNR we observed was 3, but typically it is much better than that

as shown in supplementary figure 7. Therefore, we devised a different scenario to test the robustness to noise. For the case of no noise ($\text{SNR} = \infty$) we first identified the number of iterations required for each algorithm to reach the same quality (supplementary figure 6c, 1st column). With increasing noise level we iterate the exact same number of iterations for each algorithm and analyze the output.

Supplementary figure 6a as well as 1st and 2nd row of supplementary figure 6c illustrate that the derivation based on view independence (equation 36) shows precisely the same results for sequential and combined iterations even in the presence of high noise levels. Our new derivation considering conditional probabilities between views shows minimally smaller correlations at low signal-to-noise levels (supplementary figure 6a). The differences are minimal and even at very low SNR very hard to tell apart (supplementary figure 6c). The optimizations further reduce quality, but it seems to only become relevant once the signal-to-noise level starts to drop below 3.

To compensate for noise in the deconvolution we added the option of Tikhonov-regularization. Supplementary figure 6b illustrates the influence of the λ parameter on the deconvolution results. Supplementary figure 7 shows all corresponding images for all data points. We think that although the Tikhonov regularization slows down convergence (supplementary figure 6b), a low λ might be a good choice even in environments of a high SNR (supplementary figure 7b).

10. PSF-ESTIMATION

Another common source of errors is an imprecise estimation of the PSF's. In the previous sections we always assumed to know the PSF exactly. In real life PSF's are either measured or theoretically computed and might therefore not precisely resemble the correct system PSF of the microscope due to misalignment, refractions, etc.

In order to be able to estimate the effect of using imprecise PSF's for the deconvolution we randomly rotated the PSF's we used to create the input images before applying them to the deconvolution (supplementary figure 8). We used the same scheme to analyze the results as discussed in section 9. Surprisingly, the effect on the deconvolution result is hardly noticeable for all algorithms, even at an average rotation angle of 10 degrees. The deconvolved images are practically identical (therefore not shown), the maximal difference in the correlation coefficient is $r=0.017$. We suspect that this is a result of the almost Gaussian shape of the PSF's. Although the correct solution becomes less probable, it is still well within range.

We investigated the change of the PSF of a SPIM system that should occur due to its concavity perpendicular to the light sheet across the field of view. Typical light-sheet microscopic acquisitions as shown in supplementary figure 9 and 11 show no visible sign of change, even across the entire field of view. Given the tolerance of the deconvolution regarding the shape of the PSF we concluded that it is not necessary to extract different PSFs at different physical locations. Note that the option to perform the deconvolution in blocks (section 11) would easily allow such an extension. We think that a real improvement in deconvolution quality could be achieved by being able to measure the correct PSF inside the sample.

11. IMPLEMENTATION DETAILS

The multi-view deconvolution is implemented in Fiji⁹ using ImgLib.¹⁰ Performance critical tasks are the convolutions with the PSF's or the compound kernels. We implement them using Fourier convolutions and provide an alternative implementation of the Fourier convolution on the GPU. Note that it is not possible to implement the entire pipeline on the GPU due to the limited size of graphics card memory. All significant parts of implementation including per-pixel operations, copy and paste of blocks and the Fast Fourier Transform are completely multi-threaded to allow maximal execution performance on the CPU and GPU. The source code is available on GITweb: http://fiji.sc/cgi-bin/gitweb.cgi?p=fiji.git&a=tree&f=src-plugins/SPIM_Registration. The source code relevant to the deconvolution can be found in the package `src.main.java.mpicbg.spim.postprocessing.deconvolution2`.

In practical multi-view deconvolution scenarios where datasets are acquired on light-sheet microscopes, not all views are entirely overlapping. In order to compensate for the lack of data in some areas of each view, we initially compute a weight image for each view. By default it consists of a cosine blending function¹ to avoid artifacts arising from partial overlap. The sum of weights for each pixel in the output image over all input images is normalized to 1. On each sequential update step the weight defines the fraction of what is actually changed in deconvolved image relative to each view contribution.

11.1 FIJI-PLUGIN

The multi-view deconvolution is integrated into Fiji (<http://fiji.sc>), please make sure to update Fiji before you run the multi-view deconvolution. The typical workflow consists of three steps.

1. The first step is to run the bead-based registration¹ on the data (http://fiji.sc/SPIM_Bead_Registration, [Fiji – Plugins – SPIM Registration – Bead-based registration](#)).
2. The second step is to perform a simple average multi-view fusion in order to define the correct bounding box on which the deconvolution should be performed (http://fiji.sc/Multi-View_Fusion, [Fiji – Plugins – SPIM Registration – Multi-view fusion](#)).
3. The final step is to run the multi-view deconvolution using either the GPU or the CPU implementation (http://fiji.sc/Multi-View_Deconvolution, [Fiji – Plugins – SPIM Registration – Multi-view deconvolution](#)).

Detailed instructions on how to run the individual plugins can be found on their respective Fiji wiki pages, they are summarized on this page http://fiji.sc/SPIM_Registration. Note that due to the scripting capabilities of Fiji, the workflow can be automated and also for example be executed on a cluster (http://fiji.sc/SPIM_Registration_on_cluster).

Note: An example dataset is available for download on the Fiji page: http://fiji.sc/SPIM_Registration#Downloading_example_dataset.

11.2 GPU IMPLEMENTATION

The GPU implementation based on CUDA (http://www.nvidia.com/object/cuda_home_new.html) alternatively executes the Fourier convolution on Nvidia hardware. The native code is called via *Java Native Access*. The source code as well as pre-compiled libraries for CUDA5 for Windows 64bit and Linux 64bit are provided online (http://fly.mpi-cbg.de/preibisch/nm/CUDA_code_conv3d.zip). Note that for Windows the DLL has to be placed in the Fiji directory, for Linux in a subdirectory called *lib/linux64* and that the current version of the Nvidia CUDA driver needs to be installed on the system.

11.3 BUILDING THE CUDA CODE

Using the native CUDA code is unfortunately not as easy as using Fiji. If the provided pre-compiled libraries do not work, first make sure you have the current Nvidia CUDA driver (<https://developer.nvidia.com/cuda-downloads>) installed and the samples provided by Nvidia work.

If Fiji still does not recognize the Nvidia CUDA capable devices, you might need to compile the CUDA source code (http://fly.mpi-cbg.de/preibisch/nm/CUDA_code_conv3d.zip). The supposedly simplest way is to use CMAKE, it is setup to compile directly. If, for some reason there are problems compiling it using CMAKE, you can try to compile it directly. Here is the command required to compile the CUDA library under linux, be sure to adapt the paths correctly.

```
nvcc convolution3Dfft.cu —compiler-options '-fPIC' -shared -lcudart -lcufft
-l/opt/cuda5/include/ -L/opt/cuda5/lib64 -lcuda -o libConvolution3D_fftCUDAlib.so
```


12. NUCLEI-BASED ALIGNMENT OF THE C. ELEGANS L1 LARVAE

In order to achieve a good deconvolution result, the individual views must be registered with very high precision. To achieve that, we match fluorescent beads that are embedded into the agarose with subpixel accuracy. However, in *C. elegans* during larval stages, the cuticle itself acts as a lense refracting the light sheet, which results in a slight misalignment of data inside the specimen. We therefore apply a secondary alignment step, which identifies corresponding nuclei in between views using geometric local descriptor matching,¹ and from that estimates an affine transformation model for each view correcting for the refraction due to the cuticle. The algorithm works similar to the bead-based registration^{1,6} and is implemented in Fiji as a plugin called *Descriptor-based series registration* (Preibisch, unpublished software).

REFERENCES

- [1] Preibisch, S., Saalfeld, S., Schindelin, J., and Tomancak, P., "Software for bead-based registration of selective plane illumination microscopy data," *Nat Methods* **7**, 418–9 (Jun 2010).
- [2] Lucy, L. B., "An iterative technique for the rectification of observed distributions," *Astronomical Journal* **79**(6), 745–754 (1974).
- [3] Richardson, W. H., "Bayesian-based iterative method of image restoration," *Journal of the Optical Society of America* **62**, 55–59 (1972).
- [4] Dempster, A. P., Laird, N. M., and Rubin, D. B., "Maximum likelihood from incomplete data via the em algorithm," *JOURNAL OF THE ROYAL STATISTICAL SOCIETY, SERIES B* **39**(1), 1–38 (1977).
- [5] Krzic, U., *Multiple-view microscopy with light-sheet based fluorescence microscope*, phd thesis, University of Heidelberg (2009).
- [6] Preibisch, S., *Reconstruction of Multi-Tile Microscopic Acquisitions*, phd thesis, Technical University Dresden (2011).
- [7] Temerinac-Ott, M., Ronneberger, O., Ochs, P., Driever, W., Brox, T., and Burkhardt, H., "Multiview deblurring for 3-d images from light-sheet-based fluorescence microscopy," *Image Processing, IEEE Transactions on* **21**, 1863–1873 (april 2012).
- [8] Singh, M. K., Tiwary, U. S., and Kim, Y.-H., "An adaptively accelerated lucy-richardson method for image deblurring," *EURASIP J. Adv. Signal Process* **2008** (2008).
- [9] Schindelin, J., Arganda-Carreras, I., Frise, E., Kaynig, V., Longair, M., Pietzsch, T., Preibisch, S., Rueden, C., Saalfeld, S., Schmid, B., Tinevez, J. Y., White, D. J., Hartenstein, V., Eliceiri, K., Tomancak, P., and Cardona, A., "Fiji: an open-source platform for biological-image analysis," *Nat. Methods* **9**, 676–682 (Jul 2012).
- [10] Pietzsch, T., Preibisch, S., Tomančák, P., and Saalfeld, S., "ImgLib2 – generic image processing in Java," *Bioinformatics* **28**, 3009–3011 (Nov 2012).